Sebastian Redolfi, BSc

Influence of thermal processing on the phase composition and the electrical properties of Ni-Mn-O thin films

MASTER'S THESIS

to achieve the university degree of

Diplom-Ingenieur

Master's degree programme: Advanced Materials Science

submitted to

Graz University of Technology

Supervisor

Ao.Univ.-Prof. Dipl.-Ing. Dr.techn. Klaus Reichmann

Institute for Chemistry and Technology of Materials

Graz, February 2019

AFFIDAVIT

I declare that I have authored this thesis independently, that I have not used other than the declared sources/resources, and that I have explicitly indicated all material which has been quoted either literally or by content from the sources used. The text document uploaded to TUGRAZonline is identical to the present master‘s thesis.

Date

Signature

Abstract

Negative temperature coefficient (NTC) thin films based on the Ni-Mn-O system were fabricated by chemical solution deposition (CSD). The composition of the utilized precursor solutions was fixed to a Mn/Ni ratio of 80/20 and the electrical and structural properties of the NTC thin films were investigated as a function of crystallization temperature, hold time at the top temperature during crystallization and oxygen partial pressure during crystallization and cooling.

The NTC thin films were characterized by optical microscopy, x-ray diffraction (XRD) and scanning electron microscopy (SEM) including energy dispersive x-ray spectrometry (EDS). The electrical resistance of the thin films was measured as a function of temperature and the B value calculated. The electrical stability of the NTC thin films was investigated in a 1000 h aging test where the test devices were stored at 150 °C in ambient atmosphere and the drift of the resistance after 1000 h was determined. Several intermediate measurements were performed to investigate the development of the resistance drift as a function of aging time.

Single phase nickel manganite spinel thin films were obtained by crystallizing the thin films at 900 °C in air atmosphere. Thin films crystallized at 750 °C and 650 °C in air consisted of Mn_2O_3 and nickel manganite spinel. Partial treatment in reducing atmosphere at the top temperature and during cooling led to the precipitation of a nickel rich phase, which is assumed to consist of NiO.

The electrical properties of the NTC thin films were found to strongly depend on the thermal processing conditions. The obtained B values ranged from 3470 K to 4530 K. The room temperature resistance of the thin films, determined with the help of a given electrode test structure is found between 160 kΩ and 10.6 MΩ. The resistance drift after 1000 h of aging at 150 °C ranged from 5 % to 36 %.

Kurzfassung

Über das CSD Verfahren (engl. Chemical Solution Deposition) wurden NTC Dünnschichten (engl. Negative Temperature Coefficient) basierend auf dem Ni-Mn-O System hergestellt. Die Zusammensetzung der Ausgangslösungen wurde mit einem Mn/Ni Verhältnis von 80/20 fixiert. Der Einfluss der Kristallisationstemperatur, der Haltezeit auf der Höchsttemperatur, und des Sauerstoff-Partialdrucks während des thermischen Prozesses auf die strukturellen und elektrischen Eigenschaften der NTC Dünnschichten wurde untersucht.

Die NTC Dünnschichten wurden mithilfe von optischer Mikroskopie, Röntgendiffraktometrie (XRD), Rasterelektronenmikroskopie (SEM) und energiedispersiver Röntgenspektrometrie (EDS) untersucht. Der elektrische Widerstand der Dünnschichten wurde in Abhängigkeit von der Temperatur gemessen und der B-Wert berechnet. Die Alterungsstabilität der NTC Dünnschichten wurde durch Lagerung der Test-Bauteile für 1000 Stunden bei 150 °C in Umgebungsatmosphäre getestet. Um den zeitlichen Verlauf der Alterung zu untersuchen wurde der Drift des Widerstands nach 1000 Stunden und in mehreren Zwischenmessungen bestimmt.

Einphasige Nickel-Manganat Spinell Filme wurden durch Kristallisieren der Dünnschichten bei 900 °C in Luft erhalten. Kristallisation bei 750 °C und 650 °C in Luft führte zu mehrphasigen Filmen aus Mn_2O_3 und Nickel-Manganat Spinell. Eine Behandlung der Dünnschichten in reduzierender Atmosphäre führte zu Nickel reichen Ausscheidungen von welchen angenommen wird dass sie aus NiO bestehen.

Es stellte sich heraus dass die elektrischen Eigenschaften der NTC Dünnschichten stark vom thermischen Prozess abhängen. B-Werte von 3470 K bis 4530 K, elektrische Widerstände bei Raumtemperatur von 160 kΩ bis 10,6 MΩ (gemessen mithilfe einer gegebenen Elektrodenteststruktur) und Alterungsraten von 5 % bis 36 % nach 1000 Stunden wurden ermittelt.

Acknowledgements

Zuallererst möchte ich mich herzlich bei Prof. Klaus Reichmann für die großartige Betreuung meiner Masterarbeit bedanken.

Mein großer Dank gilt der Firma TDK Electronics GmbH und Co OG für die Möglichkeit diese Masterarbeit innerhalb des Unternehmens zu erarbeiten, für die Bereitstellung von Ressourcen, Equipment und Messgeräten sowie für die finanzielle Unterstützung.

Besonders möchte ich mich bei Herrn Dr. Manfred Schweinzger, dem Leiter der Corporate Materials Research & Development Abteilung, und bei Frau Dr. Kerstin Schmoltner für die Ermöglichung, Hilfe bei der Vorbereitung und Durchführung, sowie Durchsicht der Arbeit bedanken.

Bei folgenden Mitarbeiterinnen und Mitarbeitern der TDK Electronics GmbH & Co OG möchte ich mich für Ihre Hilfe bedanken:

Thomas Resch für die Durchführung der XRD Messungen und Dr. Denis Orosel für die Hilfe bei der Auswertung derselben, Klaus Rainer für das Sputtern der Elektroden und viele gute Ratschläge, Sabine Klemen und Jürgen Melchiori für die Hilfe bei den R(T) Messungen, Helfried Perktaler für das Vereinzeln der Bauteile, Dr. Angelika Reichmann und Peter Horn für die Probenpräparation und die Hilfe bei der Durchführung der SEM Analysen. Beim ganzen Team der C R&D, im speziellen bei Kerstin, Nele, Michael, Marko, Denis, Theresa, Alexander, Thorsten, Johann und Henning für die tolle Aufnahme in das Team und viele gute und wertvolle Ratschläge.

Vielen Dank an Denise, für die Begleitung durch fast meine gesamte Studienzeit, für die schönen gemeinsamen Erlebnisse und dafür, dass du immer für mich da warst.

Ganz besonders bedanken möchte ich mich bei meiner ganzen Familie, im speziellen bei meinen Eltern Margit und Reinhard für ihre Unterstützung in allen Lebenslagen.

Table of Contents

1 Introduction

Negative temperature coefficient (NTC) thermistors are ceramic devices, usually based on semi-conductive transition-metal oxides which exhibit a decrease of resistivity with increasing temperature. NTC devices are widely used for temperature measurement and control in household, industrial and automotive applications. Other applications of NTC devices include level sensing and inrush current limitation.

Commercially available NTC thermistors are usually fabricated by standard ceramic processing routes and available down to component sizes of a few hundred microns.

The aim of this thesis was to fabricate NTC thin films based on the nickel-manganese-oxide system by chemical solution deposition (CSD) and to evaluate the structural and electrical properties of the thus processed samples. The influence of processing related parameters such as crystallization temperature and oxygen partial pressure on the properties of the thin films was investigated. Due to the comparatively high surface area and the small diffusion length, thin films represent a good model system to study the influence of those parameters. In contrast to bulk materials, it can be expected that the whole film reacts on a change of processing conditions within a reasonable short period of time.

Since the phenomenon of aging, a drift of the resistivity with time, is a reoccurring issue in the field of NTC ceramics special focus was laid on the long-term stability and reliability of the NTC thin films.

The ability to reproducibly fabricate reliable thin film NTC devices would open up possibilities for further device miniaturization beyond the limits of ordinary ceramic manufacturing. In addition, the fabrication of sensor arrays e.g. for micro-bolometer application with the help of MEMS technology is conceivable.

2 Theoretical Background

The following chapter presents the Mn-Ni-O system and its phase diagram, the spinel structure and the conductivity mechanism responsible for the NTC effect. The so-called aging of NTC materials and the possible mechanisms behind it are discussed. Additionally, an introduction to chemical solution deposition (CSD) as a processing route for ceramic thin films is given.

2.1 The Nickel Manganese Oxide System

The Ni-Mn-O system is technologically important for the fabrication of negative temperature coefficient (NTC) thermistors. For the production of bulk NTC thermistors often additional components such as Cu, Co, Zr or Fe are added to tune the electrical properties. In this thesis however, the investigation was restricted to the Ni-Mn-O system with a fixed Mn/Ni ratio of 80/20 without the addition of any dopants. This limitation was chosen to keep the system as simple as possible in order to better understand the influences of varying processing conditions.

Wickham [1] presented a phase diagram for the Ni-Mn-O system in air in 1964. A slightly extended version of the phase diagram was published by Golikov and Balakirev [2] in 1988. This diagram was the basis for the choice of the crystallization temperatures within this work and is shown in Figure 1. According to the phase diagram four different phase regions exist at different temperatures for the given composition. Up to about 700 °C a mixture of Ilmenite ($NiMnO_3$) and α-Mn_2O_3 is present. From approximately 700 °C up to slightly above 800 °C α-Mn_2O_3 and cubic spinel ($Ni_xMn_{3-x}O_4$) coexist. Above approximately 800 °C cubic spinel is the stable phase. At temperatures higher than approximately 1170 °C the spinel phase starts to decompose to $Ni_{1-x}Mn_xO$ which is as a solid solution between NiO and MnO. This decomposition leads to an increase of the manganese content of the spinel phase.

According to Györgyfalva et al. [3] the decomposition mechanism involves the formation of Mn^{3+} clusters on B sites upon heating above a certain temperature which forces the Ni^{2+} ions to occupy the energetically unfavorable A sites. This acts as a driving force for the formation of rock-salt NiO since the cation movement necessary for the transformation from spinel to NiO is very small (below 2 Å). The Mn clusters retain the spinel phase which then shows a tetragonal Jahn-Teller distortion as found in the Mn_3O_4 spinel. The decomposition of the spinel phase to a Mn rich spinel and NiO is accompanied by a release of oxygen which explains why the decomposition can, in reducing atmosphere, be observed at significantly lower temperature than stated in the phase diagram.

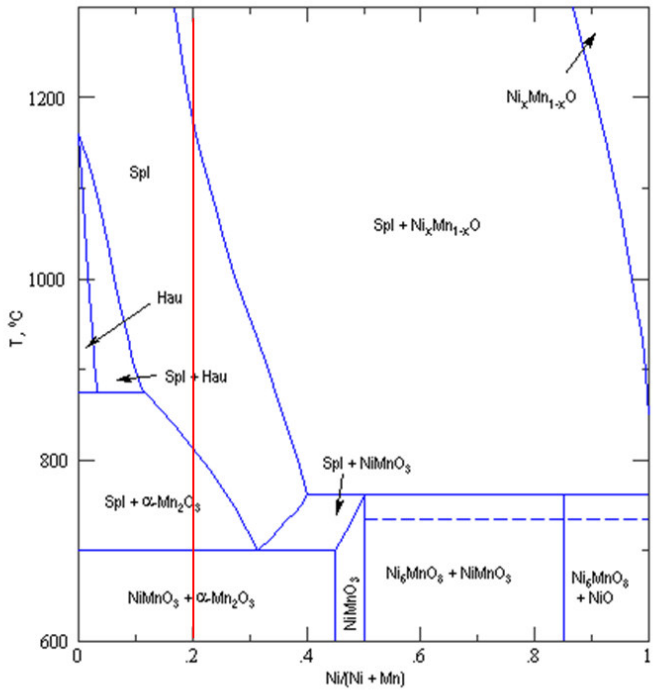

Figure 1: Phase diagram of the Ni-Mn-O system as published by Golikov and Balakirev [2] The vertical red line indicates the nominal composition of the precursor solutions used for the fabrication of the nickel manganite thin films within this thesis. Abbreviations within the figure: Spl = $Ni_xMn_{3-x}O_4$ cubic spinel; Hau = Hausmannite (Mn_3O_4 tetragonal spinel).

2.2 The Spinel Structure

Since it is generally accepted that the spinel phase is responsible for the NTC behavior of manganite spinel compounds [4–7], this phase is described in more detail in the following sections.

Following Chiang et al. [8] the unit cell of the spinel structure consists of eight face centered cubic (fcc) oxygen sub-cells arranged in a cubic 2 x 2 x 2 array. The cations occupy one eighth of the tetrahedral interstices (A sites) and one half of the octahedral interstices (B sites). In order to maintain local charge neutrality each oxygen ion is coordinated by one cation on a tetrahedral and three cations on octahedral positions. Spinel structures are often formed by transition metal oxides with the formula XY_2O_4 where X is a divalent and Y a trivalent cation. The two limiting cases regarding site occupation are the normal spinel $(X)_A(Y_2)_BO_4$ and the inverse spinel $(Y)_A(XY)_BO_4$. The subscripts A and B denote the tetrahedral and octahedral sites, respectively. In the normal spinel structure the tetrahedral positions are occupied by the divalent X cations and the octahedral positions are occupied by the trivalent Y cations. In the inverse spinel one half of the Y cations occupy the tetrahedral positions. The second half of the Y cations and the X cations occupy the octahedral

positions. At high temperature the cation distribution tends to randomize, e.g. the ratio of X/Y cations approaches 1:2 on tetrahedral and on octahedral positions. Therefore, the structure of most real spinel compounds is to some degree disordered. Figure 2 shows a schematic representation of the spinel structure.

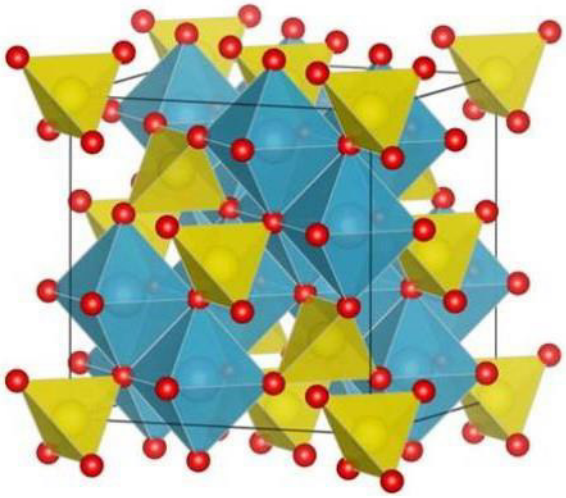

Figure 2: Schematic representation of the spinel structure. The red spheres represent the Oxygen ions. The yellow tetrahedra and the blue octahedra indicate the occupied tetrahedral and octahedral interstices, respectively. Image copied from https://crystallography365.wordpress.com/tag/spinel/, accessed 21.01.2019

2.3 Structural and Electrical Properties of Nickel Manganite Spinels

In the following a description of the spinel phase in the nickel manganite system with special respect to its electronic properties is given.

2.3.1 Conduction Mechanism

Nickel manganite spinel compounds are counted among semi-conductive oxide ceramics [4–6]. However, the conduction mechanism cannot be described adequately via the normal band picture used for ordinary inorganic semiconductors. Instead a phonon induced hopping of charge carriers via localized states between cations of the same element with different oxidation states takes place [6]. In nickel manganite spinels the charge carriers hop between Mn^{3+} and Mn^{4+} ions, both located on octahedral sites [5–7,9]. The small polaron hopping model which is explained in detail by Austin and Mott in [10] can be used to describe the conduction mechanism [7,11,12]. This model describes an electron as “self-trapped” in its own polarization field due to the strong interaction between the electron and the crystal lattice which is the reason for the low electron mobility encountered in materials with this type of conduction. The hopping is induced by lattice vibrations (phonons) and thermally activated which is the reason why the conductivity increases with increasing temperature.

2.3.2 Conductivity

Utilizing the small polaron hopping model the conductivity σ of $Ni_xMn_{3-x}O_4$ can be expressed as

$$\sigma \sim C_{Mn^{3+}} C_{Mn^{4+}} \frac{16e^2d^2}{VkT} \nu_0 exp\left(\frac{-E_a}{kT}\right) \quad (1)$$

with the fraction of $Mn^{3+/4+}$ ions on octahedral B sites $C_{Mn^{3+/4+}}$ ($C_{Mn^{3+}} + C_{Mn^{4+}} = 1$), the volume of the unit cell *V*, the distance between nearest neighbor B site cations *d*, the optical phonon frequency ν_0 and the activation energy for the hopping process E_a. As usual *e* denotes the elementary charge, *k* the Boltzmann constant and *T* the temperature [6,10,12]. Thus, the conductivity is highest for a given temperature when there are as many Mn^{3+} as Mn^{4+} ions on B sites. However, this description neglects that not every $Mn^{3+/4+}$ cation necessarily has a neighboring cation of the other valence state, and hopping conduction can only take place between cations on adjacent lattice sites. For an absolutely accurate description it would thus be necessary to incorporate the probability that no jump is possible due to the lack of a neighboring cation of the other valence state into equation (1). If the temperature dependence outside the exponential term in equation (1), which is comparatively small, is neglected, the conductivity can be expressed by an Arrhenius type law.

$$\sigma \sim \sigma_0 exp\left(\frac{-E_a}{kT}\right) \quad (2)$$

with

$$\sigma_0 \sim C_{Mn^{3+}} C_{Mn^{4+}} \frac{16e^2d^2}{VkT_0} \nu_0 \quad (3)$$

In electrical engineering and technical descriptions of NTC thermistors instead of the conductivity and the activation energy usually the resistivity ρ or the resistance *R* and the so-called B value are used to describe the electrical properties of an NTC material or device.

The temperature dependence of the resistance is often related to the resistance at room temperature (25 °C / 298 K) which is usually called rated resistance R_{25} in data sheets of devices. The resistance as a function of temperature *R(T)* and the B value are in this case defined by equation (4) [4].

$$R(T) = R_{25} \exp\left[B\left(\frac{1}{T} - \frac{1}{298}\right)\right] \quad (4)$$

The B value is defined as shown in equation (5) [4]. The unit of the B value is Kelvin. The B value is a valuable tool to gain information on the active material since it is independent of the geometrical properties of an NTC device.

$$B = \frac{E_a}{k} \qquad (5)$$

By rewriting equation (4) one obtains an expression which allows to estimate the B value from resistance measurements at two different temperatures. The relation is given in equation (6). There is no common standard which temperatures are used as a reference for the determination of *B*. Depending on the application usually the rated resistance (R_{25}) and the resistance at 100 °C or at 85 °C are utilized. Throughout this thesis the resistance values at 25 °C and 100 °C were measured to determine *B*.

$$\mathrm{B} = \ln\left(\frac{R(T)}{R_{25}}\right)\left(\frac{298 * T}{298 - T}\right) \qquad (6)$$

2.3.3 Cation Distribution

As given above (sections 2.3.1 and 2.3.2) the conductivity of nickel manganite spinels originates in the simultaneous presence of Mn^{3+} and Mn^{4+} ions on octahedral interstices. The presence of Mn^{4+} ions on B sites can be explained by the strong preference of Ni^{2+} ions for octahedral coordination in oxides. Since the divalent Ni ions are mainly located on the B sites, where they substitute a trivalent manganese ion, the charge mismatch is compensated electronically by Mn^{4+} ions [6,9].

According to Gillot et al [9] the cation distribution of $Ni_xMn_{(3-x)}O_4$ can be expressed as

$$(Ni^{2+}_{x-\alpha}\, Mn^{2+}_{1-x+\alpha})_A\, (Ni^{2+}_{\alpha}\, Mn^{3+}_{2-2\alpha}\, Mn^{4+}_{\alpha})_B\, O_4 \qquad (7)$$

where x denotes the Nickel content and α the degree of inversion of the Ni ions, the subscripts A and B stand for the tetrahedral and the octahedral sites respectively. The nominal composition of the precursor solutions within this thesis as given in section 2.1 corresponds to an x value of x = 0.6 for a pure spinel phase compound. Taking into account the considerations on the conductivity given in section 2.3.2 and equation (7) it follows that there are two main variables influencing the conductivity of nickel manganite spinels: the nickel content *x* and the degree of inversion α. The inversion parameter α is measure for the amount of Ni^{2+} ions which are, despite their preference for octahedral coordination, located on tetrahedral A sites. The inversion parameter is strongly influenced by the cooling

conditions after sintering. This can be explained as follows: At high temperatures a more random distribution of cations in the spinel structure is thermodynamically favorable. If the material is quenched the random distribution is frozen and thus α is low. Whereas when the material is slowly cooled the cations have time to rearrange themselves in a more ordered structure which is thermodynamically preferred at lower temperature. This leads to a higher α value. Additionally, the degree of inversion is not only influenced by the cooling rate but also by the atmosphere during cooling [7,12].

2.4 Aging in Nickel Manganite Thermistors

In the field of NTC ceramics the term aging refers to an increase of the resistivity over time. The extent of the aging effect depends on the composition of the nickel manganite spinel as well as on the thermal history of the material [7,11–13].

To test the aging properties usually so-called accelerated aging tests in which the samples are stored at elevated temperature are performed. For this work the samples were stored at 150 °C for 1000 h in air. The aging rate ΔR_t is usually specified in percent and calculated as shown in equation (8) with the initial resistance before aging R_0 and the resistance R_t measured after a certain time of aging *t*. In current commercially available bulk NTC devices the drift of the resistance is usually below 1 % after a 1000 h aging test.

$$\Delta R_t = \frac{R_t - R_0}{R_0} * 100\% \qquad (8)$$

The exact mechanism responsible for the aging effect is still not well understood and under discussion. Most publications agree that aging can be attributed to the redistribution of cations in the lattice and/or a partial oxidation of the ceramic [7,11,13].

Fritsch et al. [7] reported that precipitates of an oxidized, cation deficient defect spinel phase which is formed during an annealing at 850 °C followed by rapid cooling in air is responsible for the aging in $Ni_{0.76}Mn_{2.24}O_4$. The annealing was performed to simulate a common metallization treatment called serigraphy and led to a resistance decrease in comparison to the as sintered and slowly cooled ceramics. During aging at 125 °C the precipitates disappeared, and the resistance increased. The group thus proposed to perform the serigraphy treatment in nitrogen atmosphere to impede aging. No evidence for the redistribution of cations during aging experiments at 125° C was found. It was also shown that rapid cooling leads to a higher amount of Ni^{2+} ions (a lower degree of inversion) on A sites than slow cooling. The sintered and slowly (- 6 K/s) air cooled ceramic displayed almost no aging.

Groen et al. [11] found that the cationic vacancies which are formed by the oxidation of the material during fast cooling in air are not equally distributed over the ceramic, but that a higher concentration is found near the grain boundaries. The aging mechanism is described by a migration of these vacancies from the grain boundaries to the bulk and by a vacancy assisted migration of cations to their thermodynamically stable sites. The group concludes that during cooling in air the material is oxidized at the grain boundaries. The oxidation leads to the formation of cationic vacancies which diffuse into the bulk as long as the temperature is high enough. When the temperature decreases the vacancies get trapped at the grain boundaries which leads to the above described inequality in the distribution of vacancies between grain boundary and bulk. Aging at elevated temperatures then enables the vacancies to move into the bulk until they are homogeneously distributed over the ceramic. At the same time cations which are not at their thermodynamically stable sites due to the fast cooling can, with the help of the vacancies, migrate to more stable positions. This means that after a certain time of aging the ceramic should be stable and no more aging occur. If the aging temperature is set too high a simultaneous oxidation takes place and no equilibrium can be reached. A stoichiometric cooling procedure in controlled oxygen partial pressure environment is proposed to impede the oxidation of the ceramic and thus prevent aging. The case that almost no aging occurred for extremely slow air-cooled ceramics as reported by Fritsch et al. is interpreted as a limiting case where the cooling rate is so slow that a homogeneous distribution of vacancies is already reached during cooling and hence no redistribution and therewith no aging takes place.

Wang et al. [13] reported that an annealing in nitrogen at 600 °C for 24 h significantly improved the aging behavior of $Fe_{0.5}Mn_{1.84}Ni_{0.66}O_4$ NTC ceramics. The same annealing performed in pure oxygen enhanced the resistance drift. It was also shown that the electrical resistivity could be reversibly shifted up and down by subsequent treatments in nitrogen and oxygen. It is believed that annealing in oxygen favors the creation of cationic vacancies whereas the annealing in nitrogen extinguishes the vacancies. As proposed by Groen et al. the reason for the aging is attributed to the vacancy assisted migration of cations between A and B sites.

Fang et al. [12] investigated the aging properties of $Ni_xMn_{3-x}O_4$ as a function of nickel content and the thermal history of the ceramic. It was found that a higher Ni content led to higher aging of the material and that the aging of ceramics with a Ni content of $x < 0.7$ did only slightly depend on the thermal history of the material. It was reported that quenching led to higher aging than slow cooling which is explained by the higher disorder that is retained in the quenched ceramic and thus leads to a stronger tendency to cation rearrangement.

2.5 CSD Fabrication of NTC Thin Films

According to the General Introduction of the textbook by Schneller et al. [14] chemical solution deposition (CSD) processing of oxide thin films usually consists of three main steps:

- Precursor Synthesis
- Deposition
- Thermal Processing

The main demands that are made on the precursor solution are homogeneity, good wetting properties of the substrate and sufficient stability over a certain period of time (at least a few weeks). The raw materials containing the cations of interest should be well soluble in the used solvent. Ideally only the cations and oxygen should be left in the thin film after thermal processing, the solvent and any auxiliary materials should burn off. The precursor solution has to match the used deposition technique. In case of spin coating the viscosity and the evaporation rate are of special importance.

The most frequently used deposition techniques for the fabrication of ceramic thin films are spin coating, dip coating and its derivatives. Other possible techniques include aerosol deposition (spray coating) and ink-jet printing.

After deposition the film has to be dried, pyrolyzed (removal of organics) and crystallized. Depending on the material system and processing technique this can be done in a combined or in separated thermal treatments. Drying and pyrolysis are usually carried out at temperatures between 200 °C and 400 °C, crystallization at temperatures above 600 °C.

The following description of the spin coating process follows a textbook by Schneller et al. [14], chapter 11.

Spin coating is a comparatively easy and cheap technique to obtain homogenous and uniform thin film coatings on flat and smooth substrates. It consists of two major steps, the deposition of the solution, either automated as in commercial systems for mass production or manually with the help of a syringe or a pipette, and the spinning itself. During spinning fluid flow towards the edge of the substrate and solvent evaporation provide for a thin coating of the substrate's surface. The main parameters influencing the thickness of the obtained film are the set spin speed and spin time, and the concentration, viscosity and evaporation rate of the precursor solution. Typical spin speeds are a few thousand rounds per minute (rpm) and typical spin times are in the range of 30 – 60 s. Spin coating has to be performed in a clean and dust-free environment (clean room or glove box) since even small particles on the surface of the substrate could lead to defects in the deposited film.

To be suitable for spin coating substrates have to fulfill certain requirements: The substrate must be highly flat and, in the ideal case, possess a defect free surface. Any surface features, especially if they point outwards, might lead to defects in the deposited film. In addition, a substrate used for spin coating should ideally have a circular shape. If rectangular substrates are used, as was the case in this work, the edges usually exhibit a different film thickness than the remaining substrate or are not coated at all due to the flow physics of the solution.

Typical defects observed in spin coating are comets and striations. Comets originate from small particles, either on the surface of the substrate or in the solution, and lead to non- or bad covered areas from the particle outwards towards the edge of the substrate which have the form of a comet's tail. Striations are local, sinusoidal thickness variations which arise from local differences in the surface tension of the precursor solution. Additional defects that can be found especially on ceramic thin films after pyrolysis or crystallization are bursts due to the burn out of residual organics and cracks due to thermal stresses during the crystallization process.

3 Experimental

Nickel manganite NTC thin films were fabricated by chemical solution deposition (CSD) with various thermal processes. The structural properties of the obtained thin films were analyzed by optical microscopy, x-ray diffraction (XRD), scanning electron microscopy (SEM) and energy dispersive x-ray spectrometry (EDS) in SEM. The thermistor thin films were characterized electrically by resistance as a function of temperature measurements (R(T)) carried out in temperature stabilized Galden perfluoropolyether (PFPE) baths. From the R(T) measurements the B value of the thin films was calculated. Moreover, the effect of aging on the electrical properties of the thin films was investigated.

Sputtering, XRD measurements, sample preparation for SEM analysis, dicing, and R(T) measurements were partly performed by employees of TDK Electronics GmbH & Co OG.

3.1 Thin Film Fabrication

Figure 3 illustrates the necessary processing steps to fabricate NTC thin films by CSD. The individual steps are described in detail in the following sections.

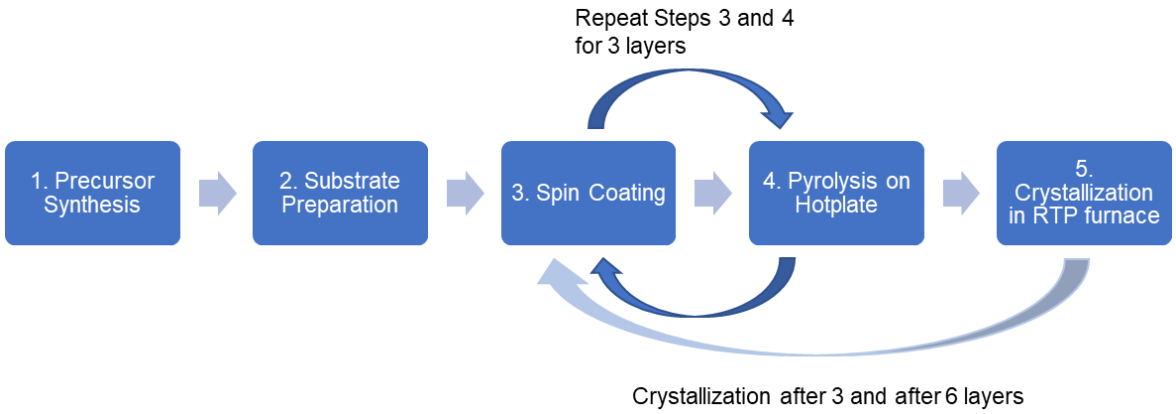

Figure 3: Necessary processing steps for the fabrication of NTC thin films by CSD.

3.1.1 Preparation of the Precursor Solutions

The precursor system utilized for the fabrication of the NTC thin films was developed based on experimental experience with precursor solutions for other material systems of TDK Electronics. 1-methoxy-2-propanol ($C_4H_{10}O_2$) was used as a solvent because it is far less toxic than the often employed 2-methoxyethanol. The main disadvantage of 1-methoxy-2-propanol is a worse long-term stability compared to solutions based on 2-methoxyethanol. However, each solution could be used for a period of two to three weeks which was regarded sufficient within this work. As a source for Mn ions Manganese(II) nitrate tetrahydrate was used, since it was found that Manganese(II) acetate tetrahydrate has a limited solubility in

1-methoxy-2-propanol. Nickel(II) acetate tetrahydrate was used to provide for Ni ions because it is much cheaper than Nickelnitrate and proofed to yield good results. The materials used for the preparation of the precursor solutions are listed in Table 1.

All precursor solutions were prepared with a concentration of 0.5 mol/L. This concentration was chosen based on preliminary experiments carried out at TDK Electronics which yielded that fabrication of good film quality is achievable with a 0.5 mol/L solution. It was found that a higher concentration of 1 mol/L leads to fringes and striations after spin coating. All precursor solutions were prepared with a composition of 80 mol% Mn and 20 mol% Ni.

Table 1: List of materials

Material	**Chemical Formula**	**CAS No.**	**Purity**	**Brand/Supplier**
Manganese(II) nitrate tetrahydrate	$MnN_2O_6 * 4\ H_2O$	20694-39-7	98.5 %	EMSURE
Nickel(II) acetate tetrahydrate	$Ni(OCOCH_3)_2 * 4\ H_2O$	6018-89-9	98 %	Sigma-Aldrich
1-Methoxy-2-propanol	$CH_3CH(OH)CH_2OCH_3$	107-98-2	>99.5 %	Sigma-Aldrich

The following equation (9) shows the calculation of the amount of materials to be weighted for the preparation of a precursor solution,

$$m = \frac{M * \mathrm{f} * c * V}{p} \qquad (9)$$

with the mass of the raw material to be weighted m [g], the molar mass of the raw material M [g/mol], the desired concentration of the solution c [mol/L], the fraction of the component in the solution f (Mn: f = 0.8, Ni: f = 0.2), the purity p of the raw material normed on 1 (1 = 100%) and the desired volume of the solution V [L].

Accordingly, first appropriate amounts of the materials were weighted (Sartorius Acculab ALC-210.4 balance; accuracy ± 0.1 mg) and transferred into a beaker. Then approximately two thirds of the required amount of solvent was added into the beaker with the help of a piston-operated pipette. The beaker was then covered with a watch glass and put into a crystallization dish filled with silicon oil which was placed on a magnetic hot plate stirrer. The silicon oil bath was used to ensure a homogeneous heating. The solution was then stirred at 300 rpm and heated to approximately 80 °C. The solid components dissolved completely after a few minutes and a bright green solution was formed. After about ten minutes at 80 °C the hotplate was switched off and the beaker containing the solution was left in the silicon oil

bath to cool for 10 to 15 minutes while continuously stirring. The beaker was then put out of the oil bath on a second magnetic stirrer and further cooled for about 15 to 20 minutes. After cooling, the solution was transferred into a 50 ml measurement cylinder and the beaker rinsed twice with a small amount of solvent. With the aid of the pipette and the measurement cylinder the solution was then filled up to the desired volume (30 or 50 ml) with an adequate amount of solvent. Since the newly added solvent did not instantaneously mix with the solution it was transferred into a new beaker and stirred for another five minutes at room temperature. The solution was then filtrated into a flask with the help of a syringe and a 0.2 µm polytetrafluoroethylene (PTFE) filter. The flask was sealed with Parafilm, wrapped in aluminum foil for light protection and stored in a desiccator.

It was found that the color of the solutions changed from bright green via dark green to brown over time. Without light protection the change of color happened within about one week. By storage under light protection this effect could be protracted for several weeks. The reason for the color change of the solution as well as its effect on film quality was not investigated within the framework of this thesis. As soon as one solution darkened significantly it was discarded and a new one prepared.

3.1.2 Substrate Preparation, Spin Coating and Pyrolysis

Polycrystalline, polished (1x1) inch aluminum oxide (Al_2O_3) wafers were selected to serve as substrates for the fabrication of the NTC thin films because of the good insulating properties of Al_2O_3. First experiments on oxide terminated silicon wafers showed that even small defects in the thin films could lead to short circuits between the top electrodes and the silicon substrate and thus yield wrong resistance measurements. Although the Al_2O_3 wafers have a good surface quality quite a number of pores and some marks from polishing were present on the surface as can be seen in Figure 4a and b which show an optical microscopy and a SEM image of a substrate. However, electrical measurability was preferred to film quality within this work. As presented in Figure 4c showing a cross section SEM image of a thin film the pores were filled but not completely closed during spin coating.

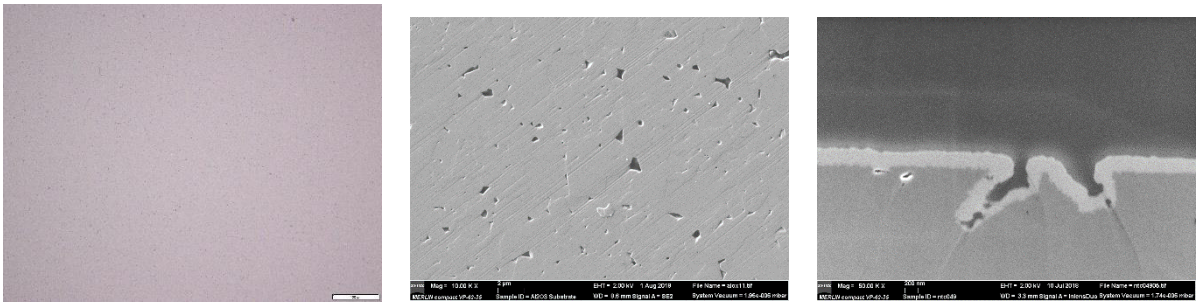

a) b) c)

Figure 4: Optical microscopy (a) and SEM (b) image of the surface of an Al_2O_3 substrate. c): SEM cross section image of a thin film. During deposition pores on the surface of the substrate are filled but not closed by the precursor solution.

The equipment used for the fabrication of the NTC thin films is listed in Table 2.

Table 2: List of processing equipment

Item	**Brand/Type**
Ultra-Sonic Bath	EMAG Technologies Emmi-05ST
Hotplate	Thermo Scientific Cimarec
Pipette	Satorius Proline Plus 1000
Spin Coater	Laurell Technologies Corporation WS-650 HZB-23NPPB
Rapid Thermal Process Furnace (RTP)	UniTemp RTP-150-EP
Oxygen Analyzer	Metrotec GSM touch oxygen analyzer
Aluminum Oxide Substrates	CoorsTek ADS 996

The substrates were rinsed with acetone followed by isopropanol. Then they were put into an isopropanol filled staining jar and cleaned in an ultra-sonic bath (USB) for 5 minutes. Starting from the USB cleaning all further processing steps were carried out in a clean room environment. After the USB cleaning the substrates were blown dry with a N_2 gun and then put on the hotplate for 5 minutes at 400 °C to enhance the wettability properties. Before the spin coating the substrates were put on a ceramic plate and allowed to cool down to room temperature.

After placing a substrate on the vacuum chuck of the spin coater it was blown clear with the nitrogen gun to remove any particles which might be on the substrate. For each layer 200 µL of precursor solution were deposited on the center of the static substrate with the help of a piston-operated pipette. After the deposition the spinning was started as soon as possible, usually within 5 s. Spin coating was performed with a spin speed of 3000 rpm and a spin duration of 30 s. The acceleration was set to 2000 rpm/s. After each layer the samples were put on the hotplate at 400 °C for 5 minutes (± 10 s) for a combined drying and pyrolysis step. Spin coating and pyrolysis were repeated for three layers. Then one crystallization step (s.

section 3.1.3) was performed. This sequence was then repeated to fabricate six-layer thick samples.

3.1.3 Crystallization Process and RTP Furnace

The crystallization of the pyrolyzed samples was carried out in a rapid thermal process furnace (RTP). The RTP furnace has a gas tight quartz glass chamber and is equipped with 24 infrared (IR) lamps with a total power of 21 kW which serve as heating elements. This allows for heating rates up to 75 K/s and top temperatures up to 1000 °C. The lamps are located at the top and the bottom of the chamber to ensure a homogeneous heat distribution within the chamber. The furnace can be run with three different process gases: nitrogen, synthetic air and forming gas. Gas flow can be set for each of the gases independently. An oxygen sensor is installed at the gas exhaust of the oven chamber which enables the measurement of the oxygen partial pressure (pO_2). As the logging of the pO_2 values had to be started manually and also manually synchronized to the automatically collected process data of the furnace the pO_2 logger was always started at the transition from the ramp up to the hold temperature. Data was recorded once per second.

Since the (1 x 1) inch substrates would fall through the standard quartz glass sample holder of the furnace a 6-inch silicon wafer with a thin layer of thermal silicon oxide on both sides was placed inside the furnace and served as an additional sample holder for the small substrates. The temperature within the furnace is measured by a thermocouple which touches the Si-wafer on its bottom side.

The pyrolyzed samples were crystallized in the RTP furnace in two steps, after three and after six layers. The different temperature profiles used are described in the following sections.

3.1.3.1 Thermal processes with five minutes hold time

The thermal processes were based on the Ni-Mn-O phase diagram (s. section 2.1). The temperatures (T) were chosen to cover the three different regions of the phase diagram present at the given composition of 80 mol% Mn and 20 mol% Ni below 1000 °C.

Temperature 1 was set to 900 °C and should yield phase pure cubic spinel films. Temperature 2 was set to 750 °C which should lead to mixed phase films consisting of cubic spinel and α-Mn_2O_3. Temperature 3 was set to 650 °C which should give films consisting of $NiMnO_3$ and α-Mn_2O_3. No spinel phase should form at this temperature according to the phase diagram. The samples were held at the top temperature for five minutes.

Since it was shown that the atmosphere during cooling affects the cation distribution and hence the electrical and aging properties of nickel manganite NTC ceramics, samples were

fabricated completely in air and with nitrogen cooling for each temperature [7]. To ensure comparability of the processes the cooling rate was set to -2 K/s. The furnace could only follow the set cooling rate for a certain time. After that the cooling rate decreased and was controlled by the heat mass of the furnace chamber. However, the cooling rate was not influenced by the gas used for cooling and only dependent on the top temperature.

The steps of the thermal process are listed in Table 3 and the time temperature profiles of two exemplary processes with 750 °C top temperature in air and with nitrogen cooling are shown in Figure 5. As stated above the temperature as a function of time curves lie exactly on top of each other for the different cooling atmospheres. The additional one-minute holding step at 200 °C was introduced to compensate for different starting temperatures of the processes due to the remaining heat within the furnace from prior run processes.

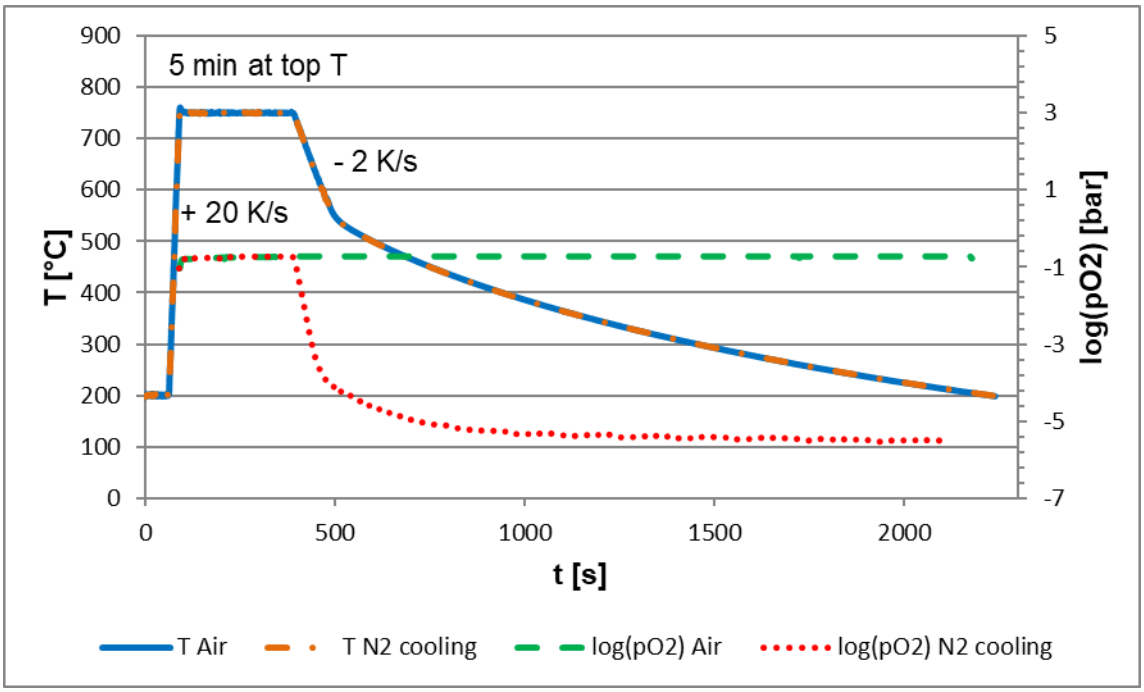

Figure 5: Exemplary thermal process with 750 °C top temperature and five minutes hold time. The continuous blue line shows the temperature for the process completely in air. The orange dash dotted line shows the temperature for the process with nitrogen cooling. The dashed green line shows the constant pO_2 for the process completely in air. The dotted red line denotes the evolution of the pO_2 for the process with nitrogen cooling.

Table 3: Thermal processes with five minutes hold time. Top temperatures: 900 °C, 750 °C and 650 °C.

Step	Description	Process gas
1	Ramp up 2 K/s to 200 °C	Air 2 L/min
2	Hold at 200 °C for 1 min	Air 2 L/min
3	Ramp up 20 K/s from 200 °C to set top T	Air 2 L/min
4	Hold at top T for 5 min	Air 2 L/min
5	Cooling -2 K/s	Air or Nitrogen 5 L/min
6	Process stop and opening of furnace at 200 °C	

3.1.3.2 Thermal processes with doubled hold time

In the course of the work for this thesis it was found that the nitrogen cooling did not significantly change neither the structural properties nor the electrical properties of the thin films in comparison to completely in air processed samples (s. chapter 4). This might be due to the long time that is required for the change from air to nitrogen atmosphere. From the change of the processing gas it took about 5 minutes until the pO_2 fell below 10 ppm (measured at the chamber exhaust) as illustrated in Figure 6. This means that the samples were not really exposed to a low pO_2 environment at elevated temperature if the gas is changed at the start of cooling.

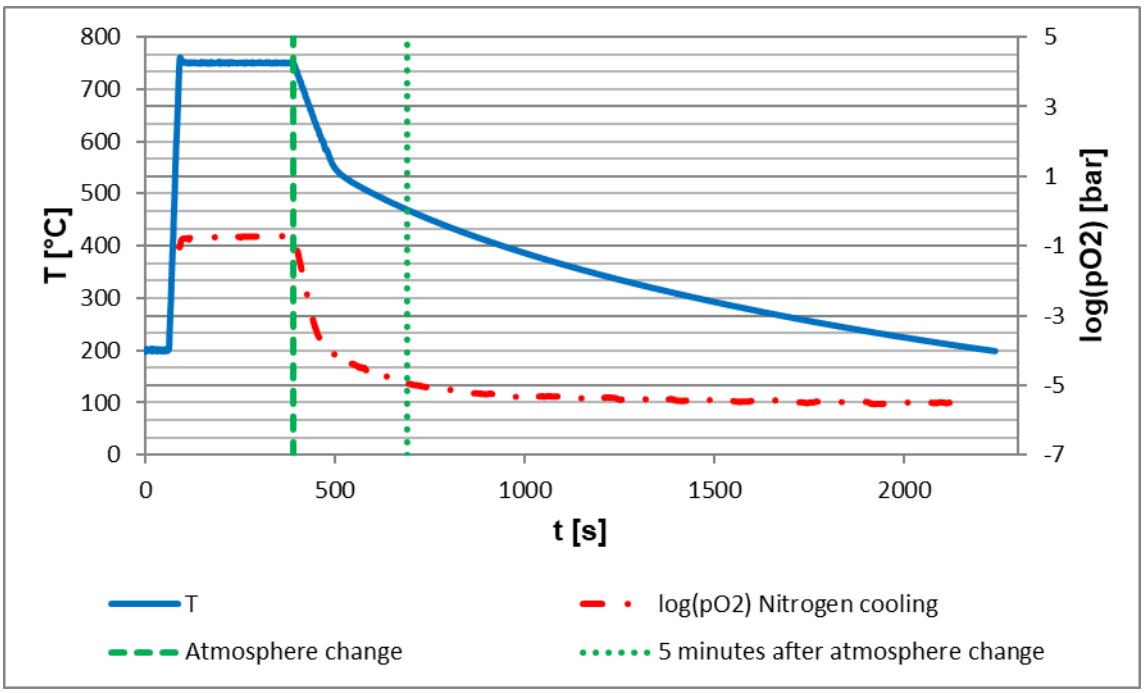

Figure 6: Time required for the change from air to nitrogen atmosphere. The continuous blue line shows the temperature for a 750 °C process with 5 minutes hold time. The dash dotted red line shows the evolution of the pO_2. The vertical dashed green line indicates the time when the process gas is changed from air to nitrogen. The vertical dotted green line indicates the point when the pO_2 falls below 10 ppm.

For this reason, a set of different processes with doubled hold time (10 minutes) and the atmosphere change from air to nitrogen after the half of the hold time was run. The top temperatures used were the same as for the experiments with 5 minutes hold time (900 °C. 750 °C and 650 °C). For comparison the processes were run completely in air as well. The process steps are described in Table 4 and the time-temperature profile of an exemplary process with 750 °C top temperature and the second half of the hold time as well as the cooling in nitrogen is displayed in Figure 7.

Table 4: Process with doubled hold time

Step	Description	Atmosphere
1	Ramp up 2 K/s to 200 °C	Air 2 L/min
2	Hold at 200 °C for 1 min	Air 2 L/min
3	Ramp up 20 K/s to top T	Air 2 L/min
4	Hold at top T for 5 min	Air 2 L/min
5	Hold at top T for additional 5 min	Air or Nitrogen 5 L/min
6	Cooling -2 K/s	Air or Nitrogen 5 L/min
7	Process stop and opening of furnace at 200 °C	

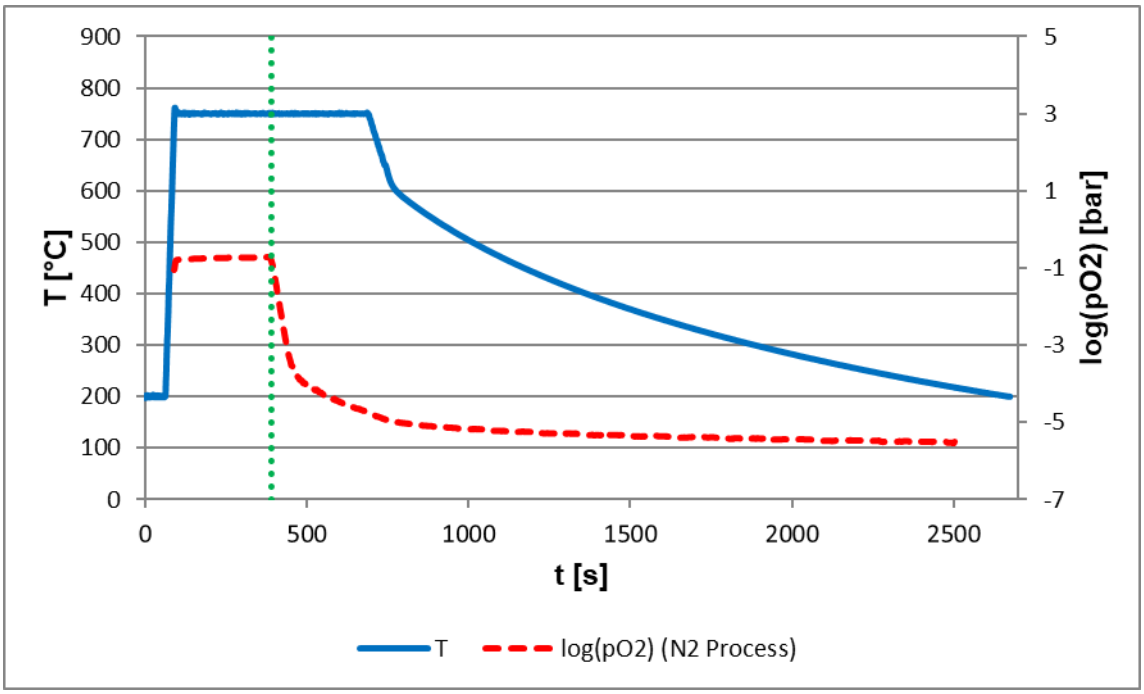

Figure 7: Exemplary thermal process with doubled (10 min) hold time and a top temperature of 750 °C. The atmosphere is changed from air to nitrogen when the half of the hold time has elapsed. The same processes were run without atmosphere change completely in air. The continuous blue line corresponds to the temperature, the dashed red line shows the pO_2 measured at the furnace exhaust for the process with change to nitrogen atmosphere. The dotted green line denotes the moment when the processing gas is changed.

3.2 Thin Film Characterization

3.2.1 Optical Microscopy

For a first quick analysis of the thin films optical microscopy images (OLYMPUS BX51M microscope and OLYMPUS Stream Motion software) were taken from each sample. The samples were investigated for homogeneity, any spin coating related defects like comets or striations and microstructure (insofar as resolvable by optical microscopy). Images were usually recorded with 50x, 200x and 1000x magnification. Unless any abnormalities or defects were found the images were taken from the center of the samples.

From the six samples fabricated with each process the four which showed the least pores and were considered the most homogeneous by optical microscopy were further prepared for electrical characterization. From the two remaining one was analyzed by XRD and the other by SEM.

3.2.2 XRD

X-ray diffraction spectra were recorded of the bare substrate and of at least one sample from each process. The samples were mounted on powder sample holders with the help of plasticine. The scans were run on a PANalytical X'Pert Pro x-ray diffractometer equipped with a Cu Kα x-ray source. 2θ scan range was set to 15 – 65°, the step size to 0.004° and the scan duration to 1 h 38 min. A 15 mm diameter incident beam mask was used. The sample was rotated in plane during the measurement.

PANalytical High Score Plus Software and PDF-2 database were used to assign the peaks to the corresponding phases and evaluate the diffraction data. Since most of the measured intensity stemmed from the aluminum oxide substrate and not from the thin film itself and because some of the Al_2O_3 peaks overlay with the spinel peaks Rietveld refinement turned out to be of no help and thus no in-depth analysis (lattice parameters, preferential orientation, etc.) of the XRD data was possible.

3.2.3 SEM

SEM investigations were carried out with a Zeiss Merlin VP Compact scanning electron microscope (SEM) equipped with a Zeiss Gemini electron column and a field emission gun (FEG), an Everhart-Thornley Detector for the detection of secondary electrons (SE), a solid-state BSE detector for back scattered electrons (BSE), an in-lens detector and an Oxford Instruments X-Max^N energy dispersive x-ray detector (EDS). EDS spectra and elemental distribution mappings were recorded with the aid of the Oxford Instruments Aztec software.

SEM images and EDS spectra of the thin films surface were recorded for one sample from each process. SEM images of the cross section of the thin films were recorded for one sample from all processes with five minutes hold time (s. section 3.1.3). To be able to record images of the cross section a special sample preparation was necessary. The sample was first scratched on the backside with a diamond pen and then broken. The fracture surface was then smoothed with an ion-mill (Hitachi IM 4000). All samples were vapor coated with a thin carbon layer before SEM analysis (C vapor coater: Jeol JEE-420).

Table 5 lists the SEM setup used to record the different images and EDS spectra/mappings.

Table 5: Parameters for SEM analysis

Parameter	**Imaging, EDS spectra and mappings**	**Surface sensitive SE imaging**	**Cross sections**
Acceleration Voltage (EHT)	10 kV	2 kV	2 kV
Aperture	60 µm high current	30 µm	30 µm
Detectors	SE, BSE, EDS	SE	Inlens, SE
Working Distance (WD)	8.5 mm	8.5 mm	3 – 6 mm

3.2.4 Sample Preparation for Electrical Measurements

In order to measure the electrical resistance of the NTC thin films as a function of temperature and hence determine the B value the samples had to be specially prepared. First inter digital electrodes were sputtered on the thin films. Then the individual electrode pads, in the following referred to as devices, were separated. The devices were then glued onto a circuit board. Electrical contact from the devices to the circuit board was established via Aluminum wire bonding. The sample preparation is described in more detail in the following sections.

3.2.4.1 Sputtering

Sputtering was performed with a Leybold-Heraeus LH Z400 magnetron sputtering system. As electrode materials, first a thin Cr layer (5 s sputtering time) to enhance adhesion was sputtered. Then an inter layer of Ni (8 s sputtering time) and a layer of Ag (6 s sputtering time) as termination were sputtered on top. The electrode materials and sputtering times were selected according to experience of TDK Electronics and were neither changed nor further investigated within the framework of this thesis.

The shape of the sputtered electrodes was realized with the help of shadow masks. Preliminary experiments were carried out to choose one of several available electrode geometries. Criteria for the selection were a high reproducibility of electrical measurements,

a sufficiently high number of individual electrode pads per sample to allow for a statistical evaluation of the measurements and a resulting resistance value which was low enough to enable good measurability.

A design-sketch of the selected sputtering mask showing the geometry of the interdigitated electrodes is shown in Figure 8a. Due to edge effects from spin coating the four devices on the edges of each wafer could not be used for electrical evaluation. Thus, five devices per sample were left to be measured. The individual devices on each substrate are named in matrix convention as indicated in Figure 8a. The nominal spacing of the inter digital electrode was specified to be 200 µm. However, it turned out that the sputtered electrodes had a mean spacing of 170 µm. An optical microscopy image of a sputtered electrode on an NTC thin film is shown in Figure 8b. Usually four samples from each process were sputtered simultaneously in one sputtering run.

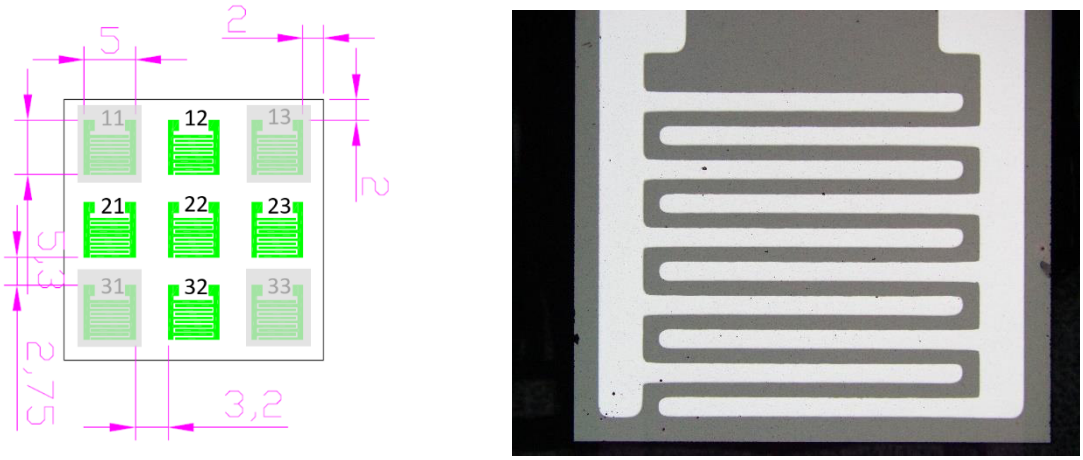

a) b)

Figure 8: a) Design-sketch of the utilized sputtering mask. The shaded pads in the corners were not used for electrical measurements. The numbers above the devices illustrate the matrix notation which is used to name the individual devices. The nominal inter digital electrode spacing of the mask is 200 µm which led to an effective spacing of about 170 µm of the sputtered electrodes. b) Optical microscopy image of a sputtered electrode.

3.2.4.2 Dicing, Gluing and Bonding

After sputtering the individual devices were separated with the help of an automated diamond disc saw (Disco DFD 6310). During sawing the samples and the dicing blade were cooled by deionized water. The individual devices were then glued on a circuit board with a silicone glue (WACKER Silicones Elastosil A07). Electrical contact between the devices and the circuit board was established via Aluminum wire bonding. (Bonder: Orthodyne Electronics). Initial problems with the adhesion of the bond-wire to the sputtered electrodes could be solved by slightly pressing the devices on the circuit board with a cotton bud directly

after applying the glue. This measure presumably impeded resilient motion of the devices during bonding and hence improved the adhesive strength of the bond.

3.2.5 Electrical Characterization and Aging

For the resistance as a function of temperature (R(T)) measurements the circuit boards including the devices to be measured were mounted on a special sample holder. This sample holder was then put into a temperature stabilized bath (LAUDA Proline RP1840) filled with Perflourpolyether (PFPE, Galden). As soon as the temperature within the bath stabilized within a window of ± 0.1 degree of the set temperature (temperature measurement: Anton Paar MKT 100 Precision Thermometer) the resistance was measured with a HP 3458 A Multimeter. R(T) measurements were performed at 25 °C and 100 °C. From each process usually 20 devices were measured (five devices from each of the four samples per process that electrodes were sputtered on).

To test the aging properties of the NTC thin films the circuit boards were put into an oven at 150 °C in ambient atmosphere. Aging was carried out for a total time of 1000 h. Intermediate measurements were performed as usual in temperature stabilized Galden baths after 16, 88, 160, 256, 496 and 1000 h. The measurement points were chosen because it is known that most NTC materials show a steep increase of the resistivity in the first period of aging which then flattens at longer aging times. A number of devices failed due to contact problems and broken bond wires after several measurements.

4 Results and Discussion

The following chapter presents the obtained results of differently processed NTC thin films and tries to give an interpretation on how they are related to the phase diagram and to theory of NTC materials in general. For the three processing temperatures, each of which corresponds to a region in the phase diagram, first the structural properties and then the electrical properties of the thin films are analyzed.

As stated in section 3.1.3 four processes were run at three different temperatures. Two with 5 min hold time, one of them completely in air, the other with a switch to nitrogen at the start of cooling, and two with 10 min hold time, again one completely in air and the other with the change from air to nitrogen at the half of the hold time. To allow an efficient comparison of those processes and to prevent confusion, a naming convention is introduced in Table 6 and kept consistently throughout the whole chapter. A detailed description of the processes is given in the experimental chapter (s. section 3.1.3).

Table 6: Abbreviations for the different processes

Abbreviation	Process
5-air	Five minutes hold time; whole process in air
5-N2-c	Five minutes hold time; change from air to nitrogen at the start of cooling
10-air	Ten minutes hold time; whole process in air
5air+5N2	Ramp up and first half of hold time in air, second half of hold time and cooling in N2

4.1 900 °C Crystallization Temperature

4.1.1 Optical Microscopy

Optical microscopy revealed no big differences between the films crystallized by the different processes at 900 °C. Figure 9 shows optical microscopy images of one representative sample from the 5-air (a) and the 5-N2-c (b) process recorded at the maximum possible magnification. Generally, no inhomogeneities or macroscopic defects like cracks were found on the samples. The microstructure of the partly in nitrogen treated samples is not as clearly visible and shows less bright islands than that of the samples treated completely in air, but in principle looks the same. The pores which can be seen in the optical microscopy images are assumed to stem from the substrate (s. section 3.1.2).

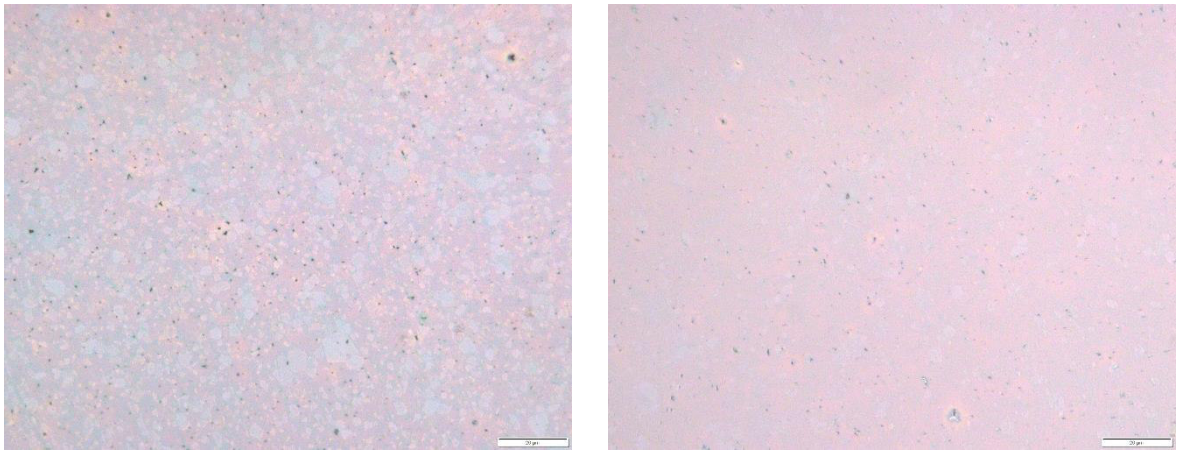

a) b)

Figure 9: Optical microscopy images of samples crystallized at 900 °C. a): typical microstructure for the 5-air and 10-air process. b): typical microstructure for the 5-N2-c and the 5air+5N2 process.
The scale bar in the lower right corner of the images corresponds to 20 µm. Magnification:1000x

4.1.2 SEM

4.1.2.1 Cross Sections

SEM images of the cross sections of one 5-air and one 5-N2-c processed sample were recorded. Except for small differences in the film thickness the cross sections look similar. An exemplary SEM image of the cross section of a 5-air sample is shown in Figure 10. The thin film is dense and no pores are observable within the film. No information on the morphology or growth mode of the films could be obtained by SEM analysis of the cross sections. Several similar images were taken along the ion-mill prepared part of the cross sections and the film thickness was measured manually with the help of the OLYMPUS Stream Motion software. The mean film thickness of the 5-air sample $t_{900\text{-}5\text{-}air}$ and of the 5-N2-c sample $t_{900\text{-}5\text{-}N2\text{-}c}$ were determined to

$t_{900\text{-}5\text{-}air} = (235 \pm 15)$ nm and $t_{900\text{-}5\text{-}N2\text{-}c} = (252 \pm 19)$ nm.

No cross section images were recorded of samples from the 10-air and the 5air+5N2 process.

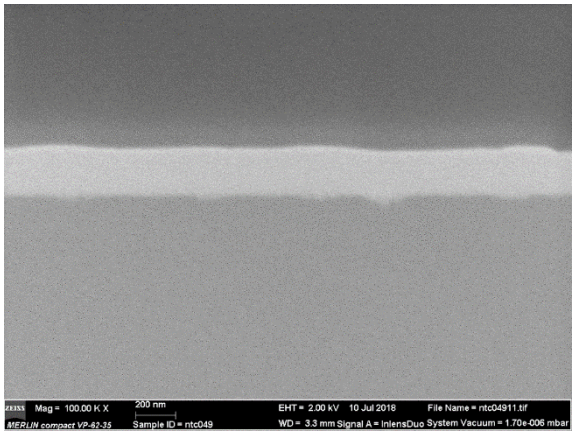

Figure 10: SEM image of the cross section of a 6 layer thick sample crystallized at 900 °C with the 5-air process. The mean thickness of the film is 235 nm. No pores or holes are visible within the film.

4.1.2.2 SEM Images and EDS – Samples Processed Completely in Air

Figure 11 displays SEM images of the surface of a sample from the 10-air process. The microstructure of samples fabricated with the 5-air process looks similar and is thus not shown here.

Generally, BSE images give mainly material contrast. In Figure 11a, however, this is to some degree deceiving. The small difference in contrast between the small grains and the bigger islands is presumably related to orientation or other factors which might influence the yield of BSE because EDS analysis showed that there is no significant difference in composition between the small and the large grains. The results of the EDS quantification for the two areas indicated in Figure 11a is given in Table 7. The quantification results show that the composition of the CSD prepared thin film is very close to the desired value of 80 at% Mn and 20 at% Ni. The EDS spectrum of area 1 is shown in Figure 12. The peaks for aluminum and oxygen were excluded from the quantification since the aluminum peak can be attributed to the substrate and oxygen is present in the substrate as well as in the film and would therefor falsify the quantification results. Carbon is generally excluded since it is present on all samples viewed in SEM and stems from the sample preparation (carbon vapor coating). The big holes in the film which are visible in the image are attributed to pores in the substrate which were not filled by the CSD process.

The SE image shown in Figure 11b was recorded with a low acceleration voltage of 2 kV to enable surface sensitive imaging and a high resolution due to a comparatively small interaction volume of the electrons with the sample. The magnification is four times higher than in Figure 11a. The surface is smooth and dense and no evidence for micro-cracks or other defects was found. The grain size of the small grains ranges from below 50 nm to approximately 200 nm. The island like big grains range from about 1 µm to several µm.

The reason for the inhomogeneous grain growth leading to the formation of the big islands was not further investigated within this work. One hypothesis is that the orientation of the grains of the polycrystalline Al_2O_3 substrate influences the crystallization of the thin film. However, this is contradicted by the fact that the number of islands is to some degree influenced by the atmosphere during processing as the samples which were partly treated in nitrogen show less islands (s. next section).

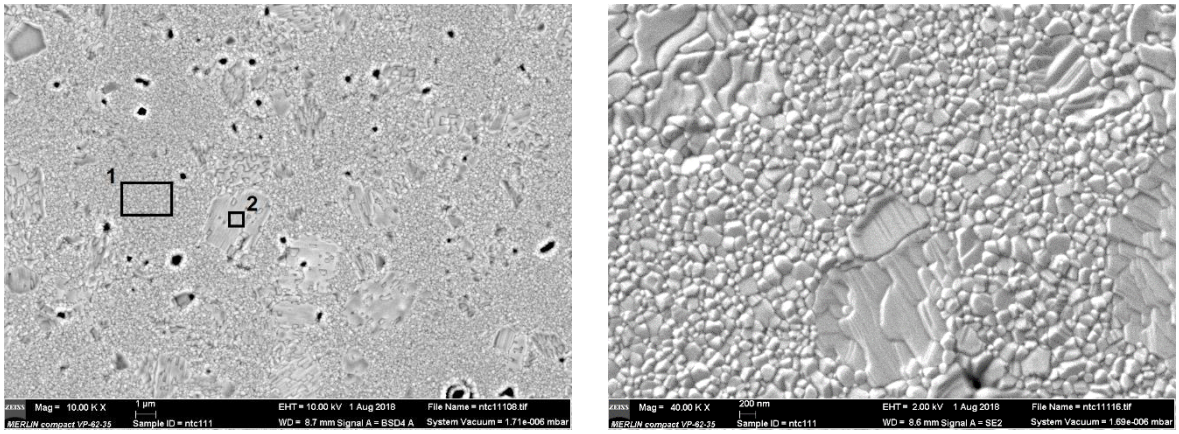

a) b)

Figure 11: a) BSE image of a 10-air processed sample. The numbered rectangles mark the areas where EDS measurements were performed. b) Low acceleration voltage SE image of the surface of the same sample at four times higher magnification than in a).

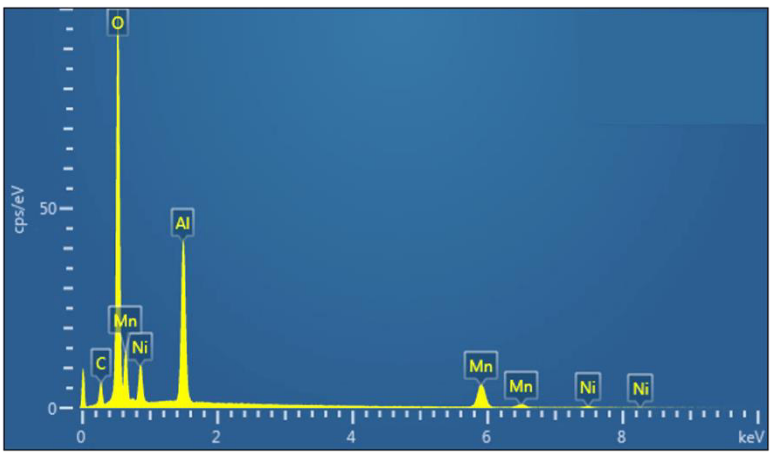

Figure 12: EDS spectrum of Area 1 from Figure 11a. The Aluminum peak belongs to the Al_2O_3 substrate, the carbon peak is due to sample preparation for SEM analysis. Oxygen is present in the substrate as well as in the film. The peaks for Mn and Ni belong to the thin film itself.

Table 7: Results of the EDS quantification from the areas indicated in Figure 11a. A measurement and quantification error of ± 2 at% is assumed.

Area	Mn [at%]	Ni [at%]
1	77	23
2	76	24

4.1.2.3 SEM Images and EDS – 5-N2-c Process

Figure 13 shows a BSE (a) and a SE (b) SEM image of the surface of a 5-N2-c processed sample. To ensure comparability the magnifications are the same as in the images of the air processed sample (s. Figure 11). The only observable difference to the air processed samples is, as already mentioned above, that there are less big, island like grains in the nitrogen cooled sample. Optical microscopy suggests that this is general the case, but no certain statement can be made since the structures are hard to see in optical microscopy and only one sample per process was investigated by SEM. The reason for the formation of these islands cannot be explained by the data gained during this work and was not investigated any further.

EDS analysis of several areas of Figure 13 gives similar results than obtained for the samples processed completely in air. The Mn content varies between 76 and 80 %, Ni content between 20 and 24 % respectively. Thus, considering the resolution of EDS and that only a minor part of the x-rays originates from the film itself, the film can be termed to be homogenous in composition.

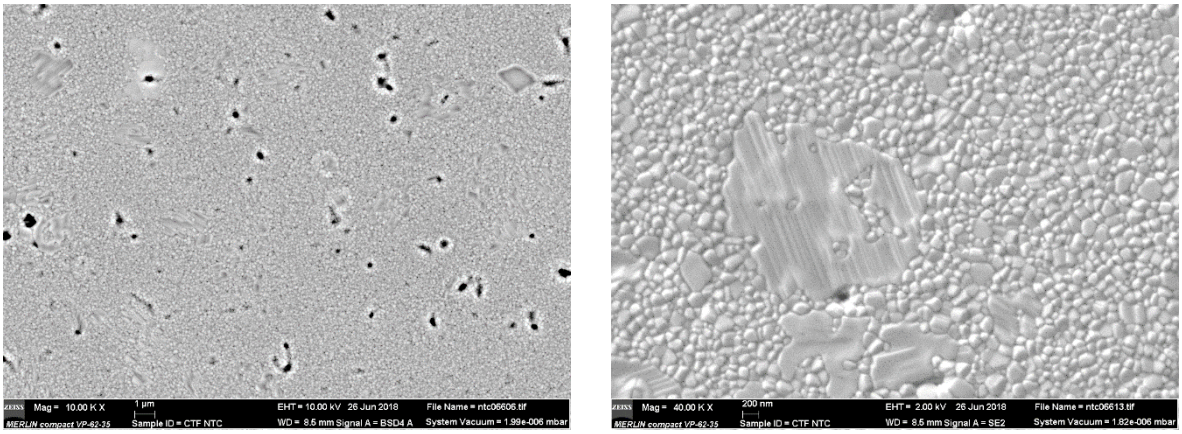

a) b)

Figure 13: a) BSE image of a 5-N2-c processed sample. There are less big, island like grains than in the air processed samples (cp. Figure 11). b) Low acceleration voltage SE image of the surface of the same sample at four times higher magnification than in a).

4.1.2.4 SEM Images and EDS – 5air+5N2 Process

Figure 14 displays SEM images of a 5air+5N2 processed sample. The microstructure obtained by this process is different than that of all other processes run at 900 °C. The small white spots visible in the BSE image in Figure 14c correspond to precipitates of a Ni rich secondary phase, most probably NiO. Due to the extremely small size of the precipitates no EDS spectrum of a single precipitate could be recorded. However, EDS measurements in a very small area around these precipitates yielded Ni contents up to 57 at% (43 at% Mn). EDS mapping also showed that the precipitates are significantly richer in Ni than the surrounding material. The precipitates are also visible as small bumps within the big grains in the SE image (Figure 14b).

The appearance of the Ni rich precipitates on the sample which was subjected to reducing atmosphere at the hold temperature and during cooling agrees with the results of Wickham and Györgyfalva who showed that the spinel phase decomposes to a Mn rich spinel and NiO above a certain temperature (s. chapter 2). Although, the decomposition should not take place at a temperature as low as 900 °C according to the phase diagram, it has to be kept in mind that the diagram was constructed in air. Wickham proposed a shift of the boarder of the spinel phase to the Ni rich side when the crystallization is performed in O_2. It appears that a shift in the other direction takes place under reducing conditions. This appears to be plausible when one considers that the decomposition of nickel manganite spinel to a Mn rich spinel and NiO is accompanied by a release of oxygen.

The fact that the Ni rich precipitates were not found on the 5-N2-c processed sample which was exposed to reducing atmosphere during cooling as well might be explained by the much shorter time which the sample is subjected to nitrogen. Additionally, during the time that is needed to change the atmosphere within the furnace chamber from air to nitrogen the samples have already cooled significantly which means that the samples are not exposed to reducing atmosphere at high temperature (s. section 3.1.3).

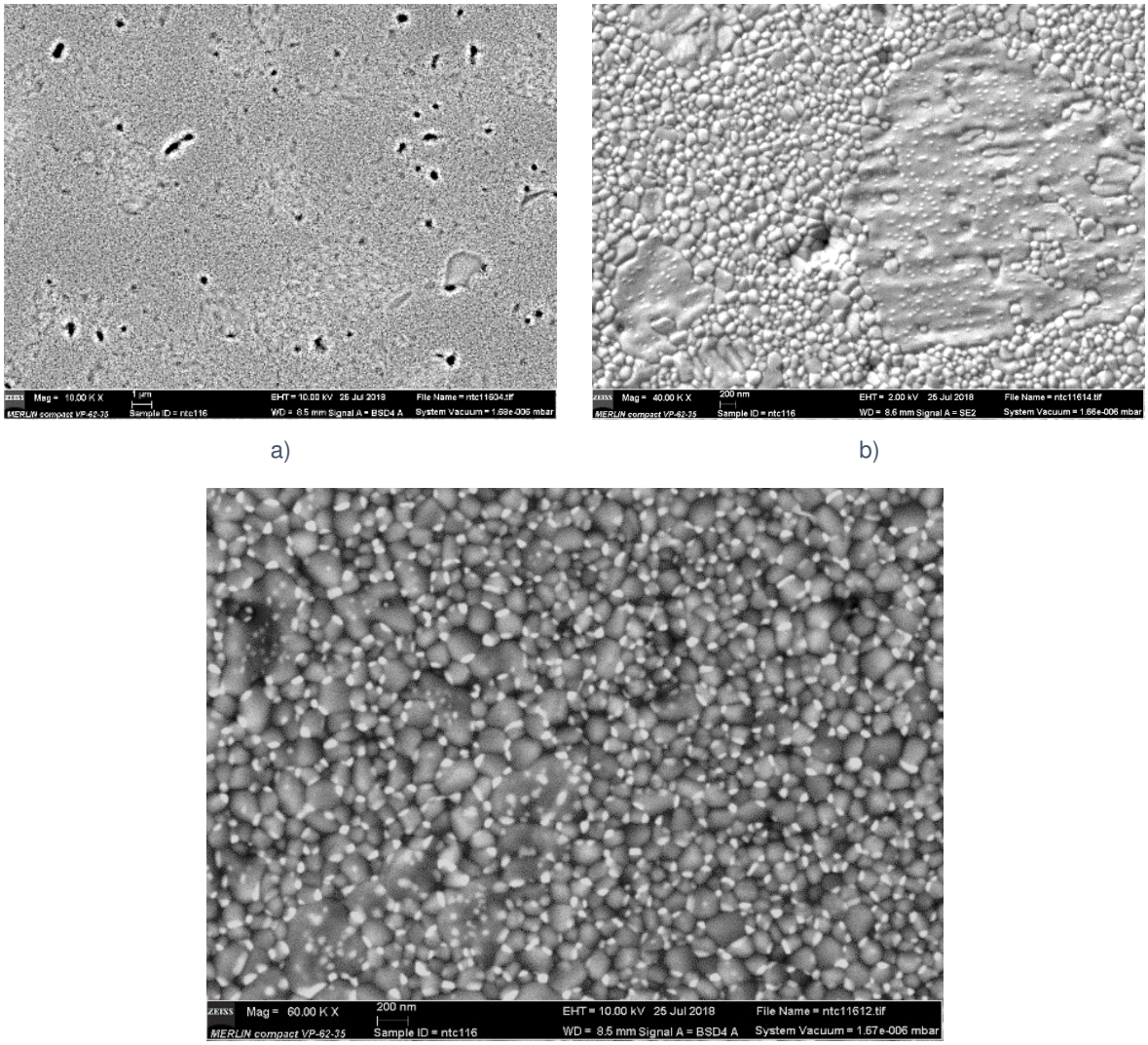

a) b)

c)

Figure 14:a) BSE image of a 5air+5N2 processed sample. b) Low acceleration voltage SE image of the surface of the same sample at four times higher magnification than in a). c) BSE image at six times higher magnification than in a). The small bumps visible on the large grains in b) and the small white spots in c) show Ni rich precipitates (presumably NiO).

4.1.3 XRD

Figure 15 shows the XRD spectra obtained from one sample from each of the four processes run at 900 °C and an XRD spectrum of a bare Al_2O_3 substrate. For the sake of clarity, the peaks were only labeled in the topmost spectrum (blue line, 5-air process). Naturally, the labelling also applies to the peaks of the lower spectrums if they are at the same position. Peaks which correspond to the aluminum oxide substrate are marked '*', peaks which can be assigned to the spinel phase are labeled 'S'. To be able to present multiple spectra in one image counts were added manually to the individual spectra. Thus, the counts scale on the y-axis does not correspond to measured, absolute counts but can only be used to compare the relative height of peaks. The highest peaks which can all be assigned to the substrate

were cut off to enable an easier observation of the smaller peaks which are of more interest since they, at least partly, belong to the thin films.

The main problem encountered during XRD analysis of the thin films was that most of the collected intensity stemmed from reflections of the substrate. For one sample the proportion of the present phases (Al_2O_3 substrate and spinel) was calculated with the aid of the PANalytical High Score Plus software. The calculation which assumes that the spectrum was obtained from a powder sample yielded a composition of about 99 % aluminum oxide and about 1 % spinel. For this reason, no Rietveld refinement und hence no calculation of the lattice parameters of the thin films was possible.

Another issue that complicates the interpretation of the XRD data which is also related to the Al_2O_3 substrates is that the main reflection of the nickel manganite spinel phase is located at an 2θ-angle of approximately 35.4 ° and thus overlaps with one of the strong aluminum oxide reflections. Additionally, the few peaks which could be used to distinguish between cubic nickel manganite spinel and cubic NiO overlap with Al_2O_3 reflections as well. Therefore, it was not possible to detect NiO by XRD analysis within this study.

As can be seen in Figure 15, all spectra obtained from the 900 °C crystallized samples display exclusively peaks which can be assigned to the spinel phase. For the samples processed in air this agrees with the phase diagram. As already mentioned above, it was not possible to prove the assumption that the Ni rich precipitates found on the 5air+5N2 processed sample by SEM correspond to a NiO phase with the help of XRD. The slight shift to lower angles of the spinel reflections in the 5air+5N2 spectrum compared to the other spectra might indicate the occurrence of a tetragonally distorted, Mn rich spinel phase. This is in accordance with the findings of Györgyfalva and Wickham on the decomposition of nickel manganite spinel by clustering of Mn^{3+} ions which retain a spinel structure and precipitation of NiO.

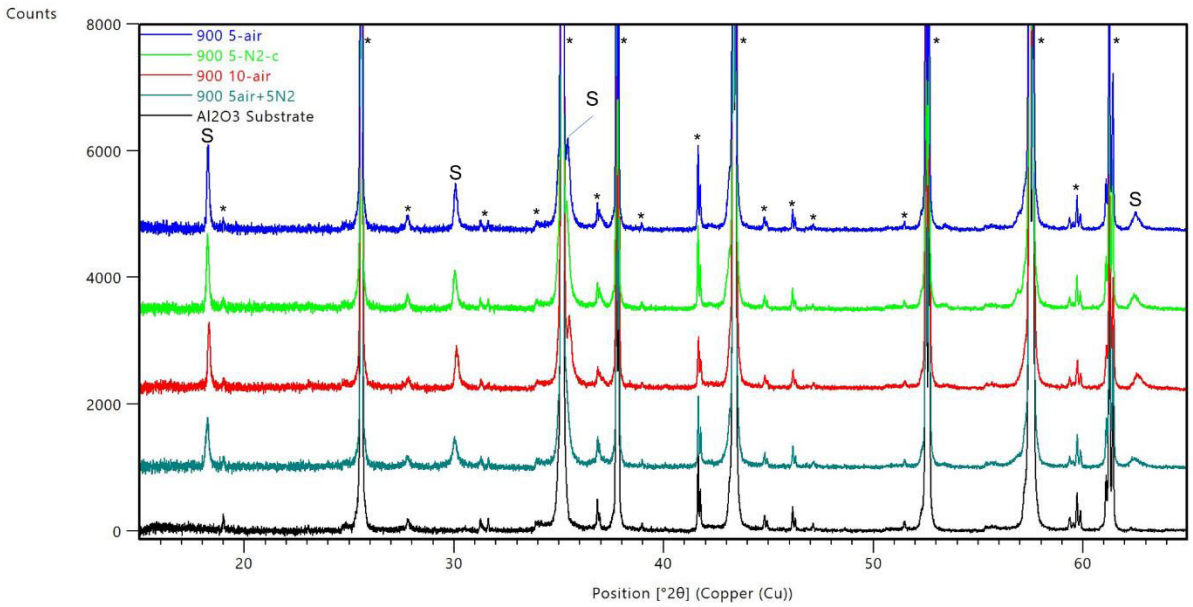

Figure 15: XRD spectra of one sample from each of the four processes run at 900 °C and a spectrum of a bare Al_2O_3 substrate (black line at the bottom). The labelling of the peaks in the topmost spectrum is valid for the spectra shown below as well. '*'denotes reflections assigned to Al_2O_3. Reflections assigned to nickel manganite spinel are labelled 'S'. To enable better comparison counts were manually added to the spectra, thus the scale on the y-axis does not give absolute measured intensity of the reflections but can only be used to compare the relative height of peaks.

4.1.4 Electrical Properties and Aging

4.1.4.1 R(T) Measurement

As described in section 3.2.5 the resistance of the devices was measured in temperature stabilized baths at 25 °C and 100 °C. In the following the resistance at 25 °C is denoted R25, the resistance at 100 °C R100. The B value was calculated from these resistance values according to equation (4). Per process 20 devices from four samples (five from each sample) were measured. It was decided that within this work the measured resistance values obtained with the electrode structure shown in Figure 8 are used to compare the different processes. The measured resistance values were not converted to the resistivity of the material because there are too many unknown parameters which would make the calculation erroneous. First of all it cannot be ascertained that the simple relation that the resistivity equals the resistance times the active area divided by the length of the conducting region is at all valid for the given case. In addition, accurate thickness measurements exactly at the position of the electrodes and measurements of the electrode spacing of each individual device would have been necessary to allow for a calculation with low enough error to ensure comparability of the different processes. Considering this it was resigned to calculate the resistivity. The data presented in the following thus gives an overview of what range of electrical characteristics can be achieved by utilizing an identical CSD process, just varying

the conditions of the thermal crystallization process and allows for a qualitative comparison of the processes. However, the data does not give direct information on the material property resistivity because process related differences in film thickness and film morphology are not considered. Naturally, the above stated applies to the electrical properties of the films crystallized at 750 °C and 650 °C as well.

Figure 16 shows the resistance values measured at 25 °C (a) and the calculated B values (b) of the samples fabricated at 900 °C. The diagrams are subdivided into four sections each of which corresponds to one of the four processes. The individual samples of each process can be distinguished by the color and shape of the data points. Each of the five data points of one sample corresponds to the measured resistance value of one device cut out from this sample. For every sample the data points are arranged in the same order and correspond to the devices as follows: From left to right: device 12, 21, 22, 23 and 32. Figure 8 in section 3.2.4.1 shows the naming convention of the devices and where they are located on the sample. If there are less than five data points for a sample this means that either a bond wire broke during or before the measurement or that the measurement did not work correct due to contact problems which sometimes occurred. This arrangement allows to compare the data obtained from the different processes but also to evaluate the spreading of the values between the samples of one process and between the individual devices of one sample. The data obtained from the samples fabricated at 750 °C and 650 °C was arranged alike and is presented in sections 4.2.4 and 4.3.4.

No evidence for a correlation between the measured resistance and the position of a device on a sample was found. The devices from the sample's center (device 22) sometimes show higher, sometimes lower resistance than the four devices located nearer to the edge of the sample. This implies that there is no systematic thickness gradient from the center outwards on the thin films. Depending on the process and the crystallization temperature either the spreading of the individual devices of one sample or the spreading of the different samples between each other is greater. This is shown well by the resistance values of the 5-air and the 5air+5N2 samples crystallized at 900 °C as given in Figure 16a. The resistance spreading of the 5-air process is governed by the spreading of the individual devices whereas for the 5air+5N2 process each sample seems to have its own mean value around which the resistance values of the individual devices are distributed.

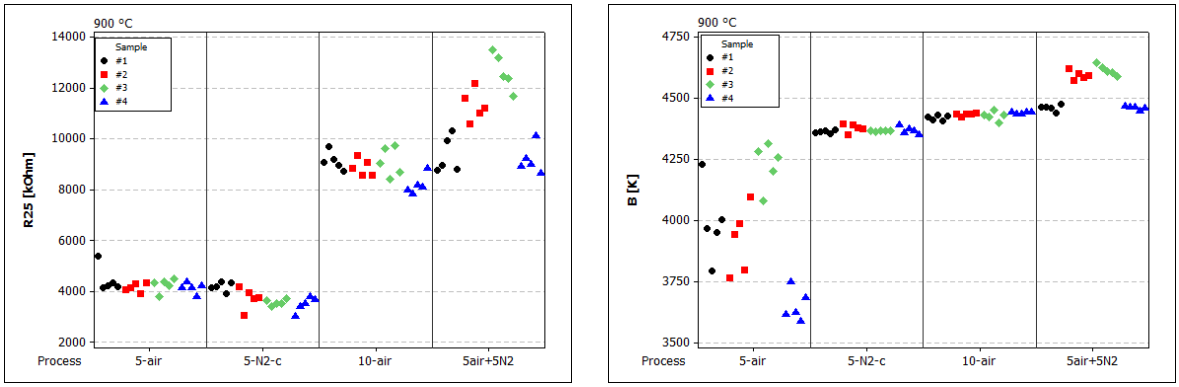

a) b)

Figure 16: a) Resistance of the samples processed at 900 °C measured at 25 °C. Each vertical section of the diagram corresponds to one process. The individual samples of each process can be distinguished by the color and shape of the data points. The devices belonging to one sample are arranged from left to right: device 12, 21, 22, 23, 32. b) Shows the corresponding B values calculated from the resistance at 25 °C and 100 °C.

As can be seen in Figure 16 there is no significant difference between the R25 values of the 5-air and the 5-N2-c processed sample. This agrees with the results of the structural characterization which did not show differences between the thus processed samples either. The extreme spreading of the B values of the 5-air processed samples which stems from a wide spreading of the R100 values could not be explained. First a measurement error was assumed but a repetition of the measurement yielded similar results. It is interesting that there is not much difference between the R25 and B values of the 10-air and the 5air+5N2 process since significant structural differences between the two processes were observed, whereas nearly no structural differences were observed between the five-minute hold time processes and the 10-air process. The 10-air process at 900 °C is the only 10-air process which shows this deviation from the five minute processes. The 10-air processes run at 750 °C and 650 °C yielded similar results than the five minute processes at the respective temperature (s. section 4.2.4.1 and 4.3.4.1). A definite reason for this behavior cannot be given at this point, since SEM analysis did not reveal differences in the morphology, e.g. significantly larger grains and XRD did not show any significant differences either.

It is quite remarkable that the 10-air and the 5air+5N2 processed samples display relatively similar resistance. Due to the Ni rich precipitates in the samples fabricated with the 5air+5N2 process the spinel phase in this samples must be richer in manganese than the spinel phase in the 10-air samples, which at the given composition should lead to an increase of the material's resistivity.

4.1.4.2 Aging

Figure 17 shows the drift of the resistance calculated as stated in equation (8) as a function of aging time for the samples processed at 900 °C. Each line represents the development of

the resistance of one individual device that was subjected to the aging test. The results of devices which failed at some point of the aging test, mostly due to broken bond-wires, were excluded from the plots.

One part of the devices from the 5-air and the 5-N2-c processes show a rather steep increase, the other part and almost all devices from the 10-air and the 5air+5N2 processes a decrease of the resistance within the first 16 hours of the aging test. This is remarkable since an increase of the resistance would have been expected for all devices. The reason of this behavior cannot be explained at this point and will be topic of future research. From 16 hours on, the devices of the 5-air and the 5-N2-c processes display a rather normal aging behavior showing a steady increase of the resistance. The devices of the 10-air and the 5air+5N2 process show an alternating in- and decrease of their resistance up to 250 hours. It is hard to judge whether this data represents the actual aging behavior of the ceramic or whether it is mainly influenced by erroneous measurements. Since the resistance of the devices from these two processes is very high, which sometimes led to problems during the measurements and because the in- and decrease ranges within a few percent of the resistance the second option seems more likely.

After 1000 hours the 5-air and the 5-N2-c processed devices display the highest aging. The resistance drift of the 5-N2-c fabricated devices is slightly lower than that of the 5-air devices but regarding the spreading of the individual devices of each process this difference cannot be considered significant. Both processes do not show a noticeable flattening of the aging curves with increasing aging time which implies that no equilibrium is reached and that the resistance drift would further increase if the aging test was continued.

The resistance drift after 1000 hours of the devices from the 10-air process is significantly lower than that of the 5 min processes. In addition, a flattening of the aging curve can be observed for at least some of the devices. The 5air+5N2 processed devices display an even lower resistance drift after 1000 hours of aging.

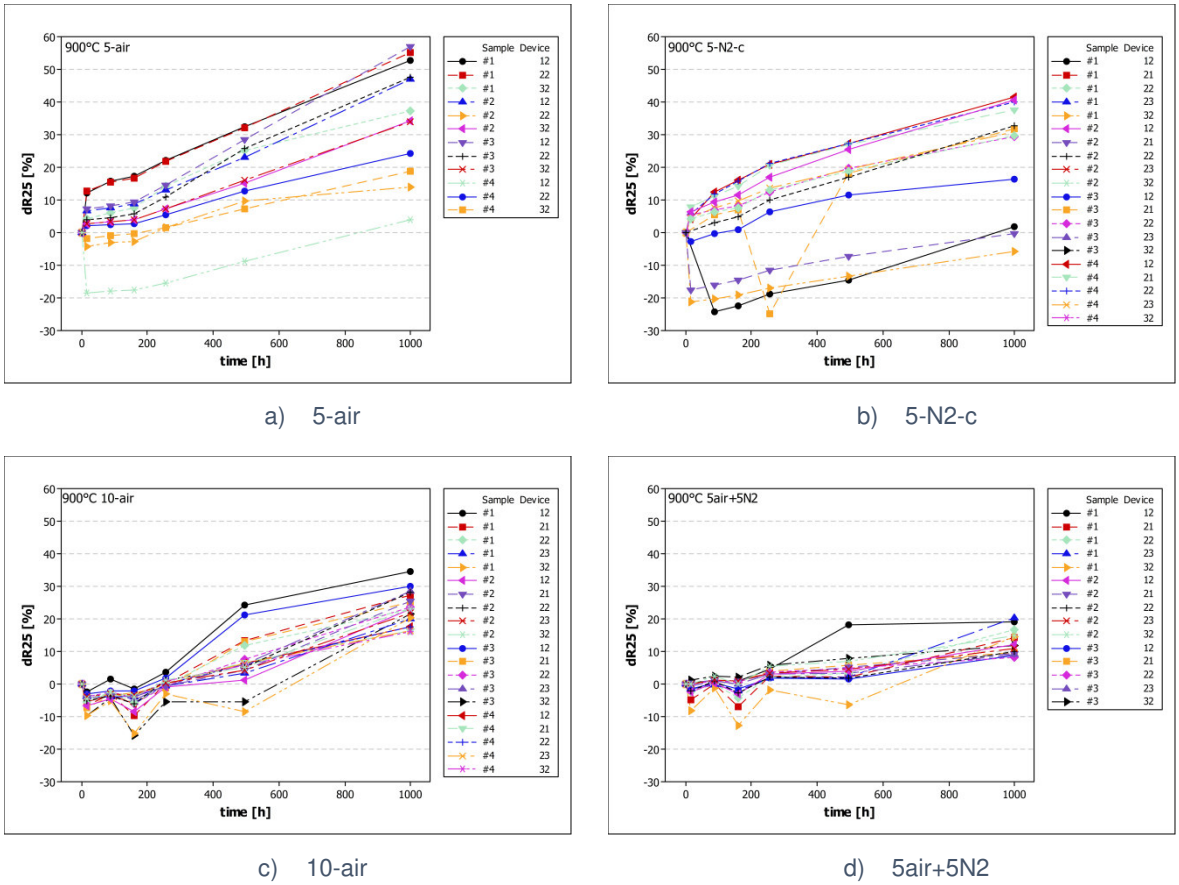

a) 5-air b) 5-N2-c

c) 10-air d) 5air+5N2

Figure 17: Resistance drift of the samples fabricated by the different processes at 900 °C as a function of aging time.

Figure 18 shows the corresponding drift of the B values calculated like the drift of the resistance. The change of B shows to which extend the slope of the R(T) curve changes during the aging test. The in- and decrease of ΔB within the first 250 hours as shown by the devices of the 10-air and the 5air+5N2 process which exactly resembles the development of the ΔR25 of these processes indicates that, as already stated above, there might have been some problem with the measurement of the R25 since the R100 obviously behaves differently. The jump of the B value of the samples from the five-minute hold time processes within the first 16 hours of the aging test suggests that some change in the ceramic or at the ceramic electrode interface takes place when the device is subjected to elevated temperature for the first time. No detailed explanation of this effect can be given at this point.

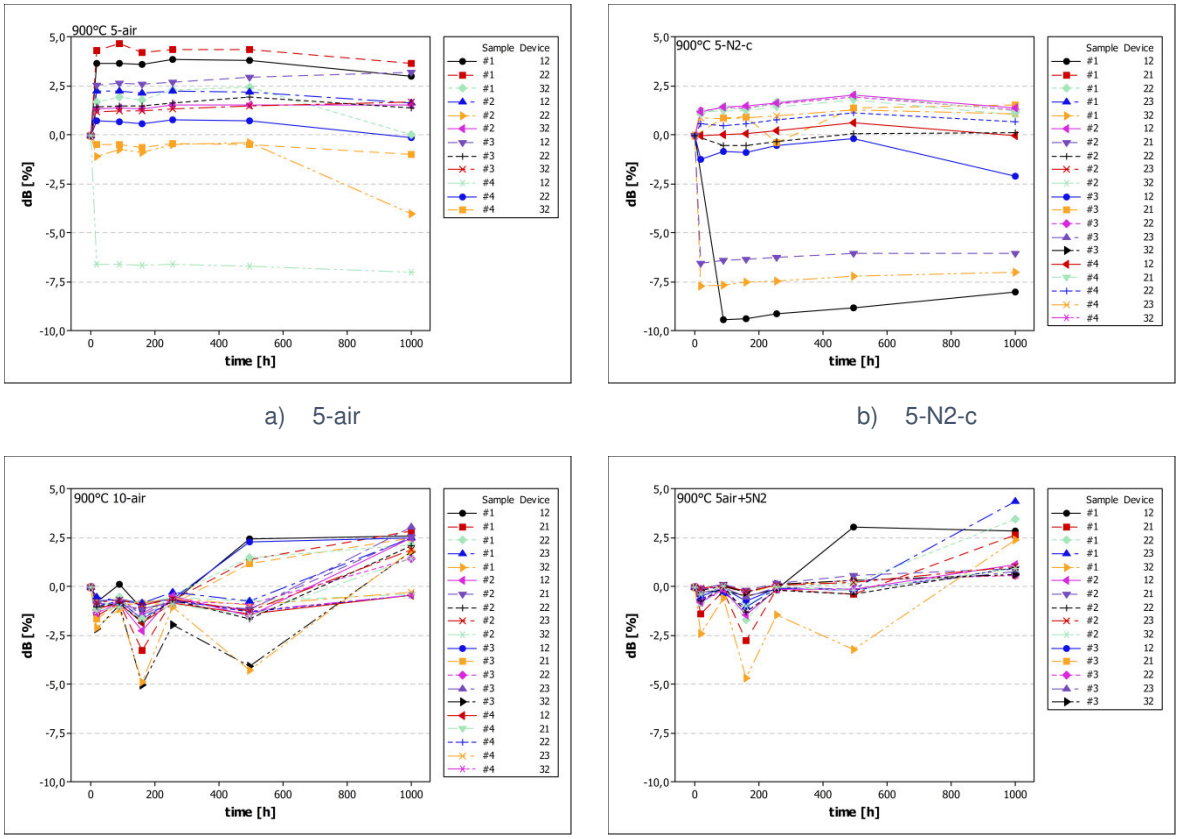

a) 5-air b) 5-N2-c

c) 10-air d) 5air+5N2

Figure 18: Drift of the B-value ΔB of the samples fabricated at 900 °C as a function of aging time.

4.2 750 °C Crystallization Temperature

4.2.1 Optical Microscopy

In general, optical microscopy of the samples crystallized at 750 °C yielded that the thin films are not as homogeneous as the ones crystallized at 900 °C. Some samples showed slightly brighter and darker areas which are also visible with the unaided eye when the sample is viewed in the right angle against a light source. Figure 19 shows optical microscopy images recorded on differently appearing areas of the same sample. The appearance of these darker and brighter areas is investigated in more detail in the chapter on the 650 °C crystallized samples (s. section 4.3) since the effect was observed even stronger on this samples.

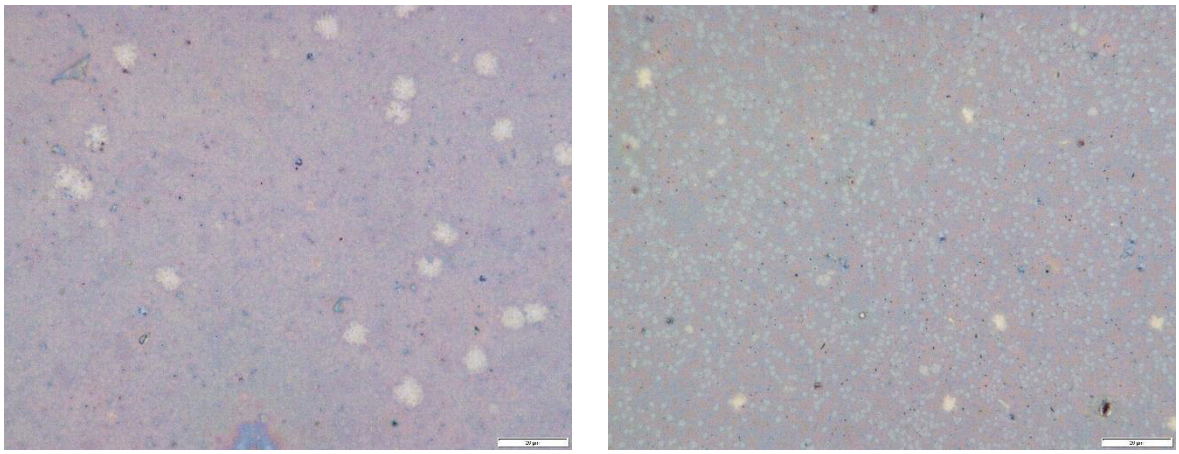

a) b)

Figure 19: Optical microscopy images of different areas on the same 5-air processed sample at maximum possible magnification (1000x). a) Brighter appearing area. b) Darker appearing area. The scale bar corresponds to 20 µm.

Basically, the optical microscopy images of the samples processed with the 5-air, 5-N2-c and 10-air processes look very similar, with the exception that the 5-air samples show a higher number of the bright white spots. The optical microscopy images of the 5air+5N2 processed samples look different as can be seen in Figure 20. In addition to the differently appearing structure no brighter and darker areas and only very few of the white spots were observed on samples of this process.

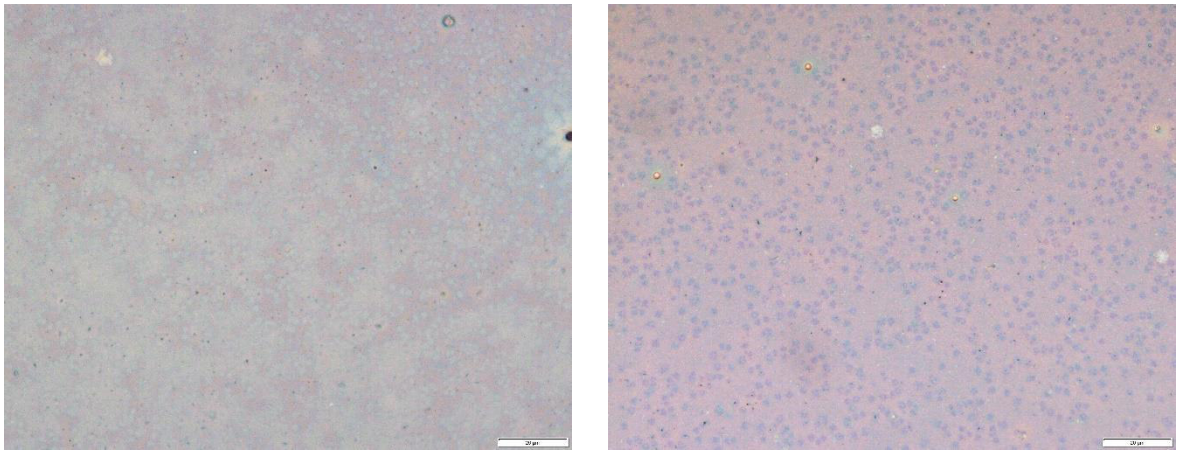

a) b)

Figure 20: a) Optical microscopy image of a 5-N2-c processed sample recorded in the transition region between a bright and dark appearing area. b) Image of 5air+5N2 processed sample. Both images were recorded at maximum magnification (1000x). The scale bar corresponds to 20 µm.

4.2.2 SEM

4.2.2.1 Cross Sections

Like for the 900 °C crystallized thin films, SEM images of the cross section of one 5-air and one 5-N2-c processed thin film crystallized at 750 °C were recorded. Again, no images of cross sections from 10-air and 5air+5N2 processed films were taken.

In contrast to the films crystallized at 900 °C the samples processed at 750 °C show some pores within the film. At some positions the films are dense and only some small pores can be seen, at other positions the pores extend along the film for several hundred nanometers. This is illustrated in Figure 21. The fact that the pores are nearly exclusively found near the center of the film suggests that the pores are due to the two separated crystallization steps after three and after six layers. It seems that during crystallization at 900 °C diffusion is strong enough that the fourth layer binds to the already crystallized layers below whereas at lower temperatures the sintering is not completed.

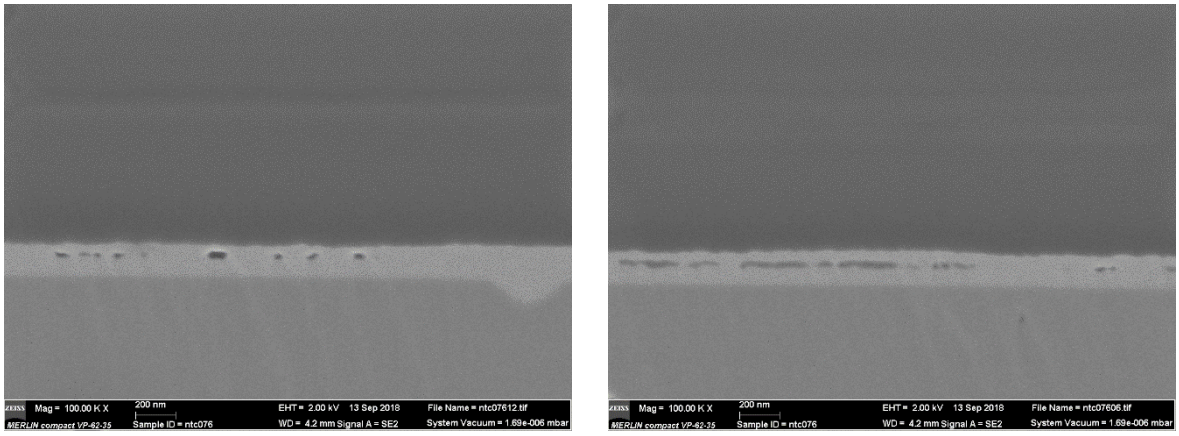

a) b)

Figure 21: SEM images of a 5-N2-c processed sample recorded at different positions of the cross section. a) Small pores within the film. b) Several hundred nanometer long pores within the film.

The film thickness was again determined at several positions along the ion mill prepared surface yielding:

$t_{750\text{-}5\text{-}air} = (225 \pm 13)$ nm and $t_{750\text{-}5N2\text{-}c} = (170 \pm 17)$ nm

It is curious that the nitrogen cooled film is significantly thinner than the film fabricated in air and also than the films crystallized at 900 °C. It would have been expected that the thickness of the films processed at 750 °C with the different processes does not differ significantly and that the films are slightly thicker than the films fabricated at 900 °C since they contain a certain pore volume. The reason for the differences in thickness and whether these results are reproducible will be topic of future work and cannot be explained at this point.

Except for the different thickness no differences between the cross sections of the 5-air and the 5-N2-c processed films were found.

4.2.2.2 SEM Images and EDS – 5-air and 5-N2-c Process

A BSE image including the areas where EDS spectra were recorded and a SE image of a 5-N2-c processed sample are shown in Figure 22. The results of the quantification of the EDS spectra are given in Table 8. The BSE image and the EDS quantification show that the thin film consists of two phases which are different in their chemical composition. One phase is richer in Ni content and seems to be more coarse-grained and porous. The other, which appears to be more dense shows a lower Ni content. XRD measurements (s. section 4.2.3) confirmed that a second phase, namely Mn_2O_3, is present in addition to the spinel phase. The formation of Mn_2O_3 leads to enrichment of Ni in the spinel phase. Thus it can be said that the Ni rich phase corresponds to the spinel, the Ni poor phase mainly to Mn_2O_3. That the Ni content does not go to zero in the areas which presumably correspond to Mn_2O_3 can

either be explained by the fabrication in layers which might lead to a spinel and a Mn_2O_3 phase on top of each other or, since the measured areas are quite small by the interaction volume of the primary electrons within the sample. Due to the difference in morphology the two phases can also be seen separately in the SE image. A comparison of the SE image in Figure 22b to the images of the samples crystallized at 900 °C (Figure 13b and Figure 14b), shows that the grains are generally smaller for the lower crystallization temperature which is in accordance with basic thermodynamics. Please note that the magnification of the images is different.

The spectrum of area 6 showed a significant peak for Mg. Therefore area 6 was omitted in the quantification since it cannot be assumed that the result of the quantification routine which only considers Mn and Ni is correct. Small grains which contain Mg and have a similar appearance as the grain below area 6 were also found in other samples. Whether the Mg is due to some contamination in the film or in the substrate could not be ascertained during SEM analysis.

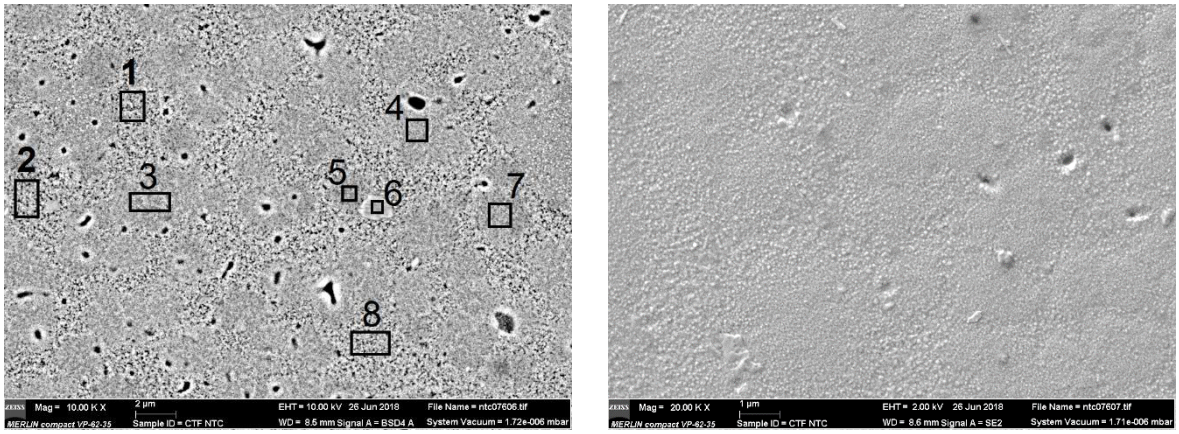

a) b)

Figure 22: a) BSE image of a 5-N2-c processed sample. The numbered rectangles indicate where EDS spectra were recorded. b) Low acceleration voltage SE image of the same sample at twice as high magnification than in a).

Table 8: Quantification results of the EDS spectra corresponding to the areas shown in Figure 22a. Area six was excluded since it was found that it contains Mg which was not considered in the quantification routine an thus the result is falsified for this area. A measurement and quantification error of ± 2 at% is assumed.

Area	Mn [at%]	Ni [at%]
1	75	25
2	74	26
3	80	20
4	80	20
5	84	16
7	84	16
8	74	26

Figure 23 shows a BSE image and an EDS mapping of the Ni L line of a 5-air processed sample. In principle the microstructure looks similar to the 5-N2-c process. The only differences are the circular shapes that can be seen in the upper part of the image which might correspond to the white spots found in the optical microscopy images of the 5-air processed samples. The chemical composition of these circles does not deviate significantly from the remaining parts of the sample. The reason for the formation of the circular shapes could not be discovered within this work. The different phases visible are the same as found on the 5-N2-c processed sample. EDS quantification yielded a Ni content between 13 at% and 33 at% in the different phases which is a slightly greater range than found in the 5-N2-c sample. The EDS mapping in Figure 23b visualizes the distribution of the different phases. The Mn rich phase tends to cluster in approximately equiaxed areas. The Ni rich phase fills the areas in-between.

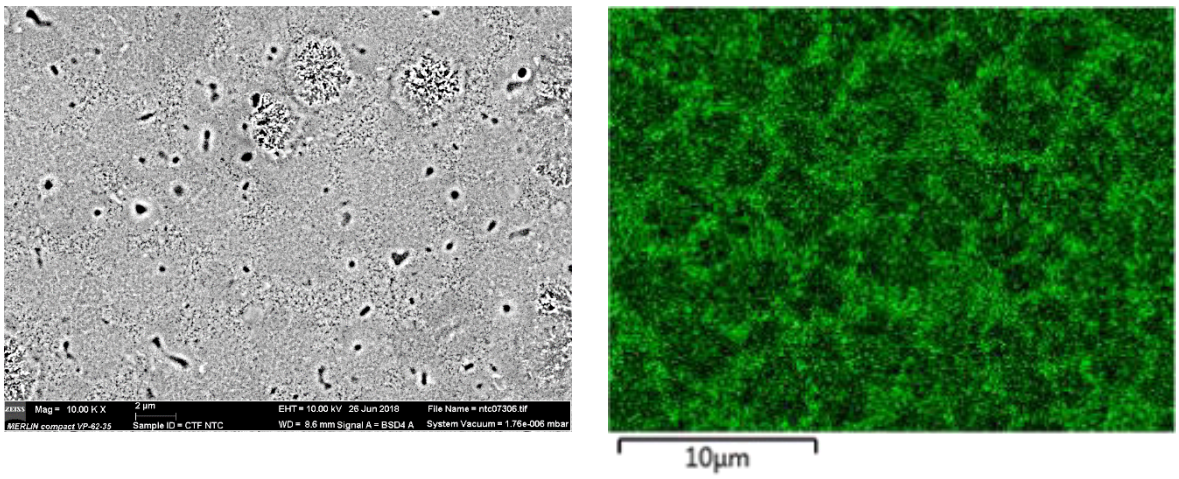

a) b)

Figure 23: a) BSE image of a 5-air processed sample. The circular shapes in the upper part of the image might correspond to the white spots observed in optical microscopy. b) EDS mapping of the Ni L line of the sample area shown in a).

4.2.2.3 SEM images and EDS – 10 air and 5air+5N2 process

Figure 24a shows a BSE image of a 10-air processed thin film, which looks similar to the images of the 5-air and 5-N2-c process. Please note that the image shown here was recorded with doubled magnification in comparison to the images shown in Figure 22 and Figure 23. EDS, as well, yielded similar results as found for the two five-minute hold time processes. The areas appearing denser in the image are richer in manganese, the areas which look more porous are richer in Ni. The Ni content varies between 13at% and 29 at%.

Figure 24b and c show BSE images of a 5air+5N2 processed sample at different magnification. Like all other samples treated at 750 °C the images show two differently appearing areas, but the morphology is different than observed for the other processes. The areas which correspond to the Ni rich phase of the other processes are denser and more coarse-grained. Higher magnification (c) reveals small Ni rich precipitates, like the ones already found with the 5air+5N2 process at 900 °C. It is again assumed that these precipitates consist of NiO. EDS measurements were performed on this sample as well, but did not give meaningful results since the signals from the Ni rich precipitates and the remaining film overlap. Thus, no reliable determination of the Ni and Mn content in the various areas is possible. XRD (s. section 4.2.3) revealed that no Mn_2O_3 is found in the samples fabricated with the 5air+5N2 process at 750 °C. A hypothesis on how the structure of this films develops during crystallization, summing up the knowledge gained from SEM and XRD, is given in the following section on XRD.

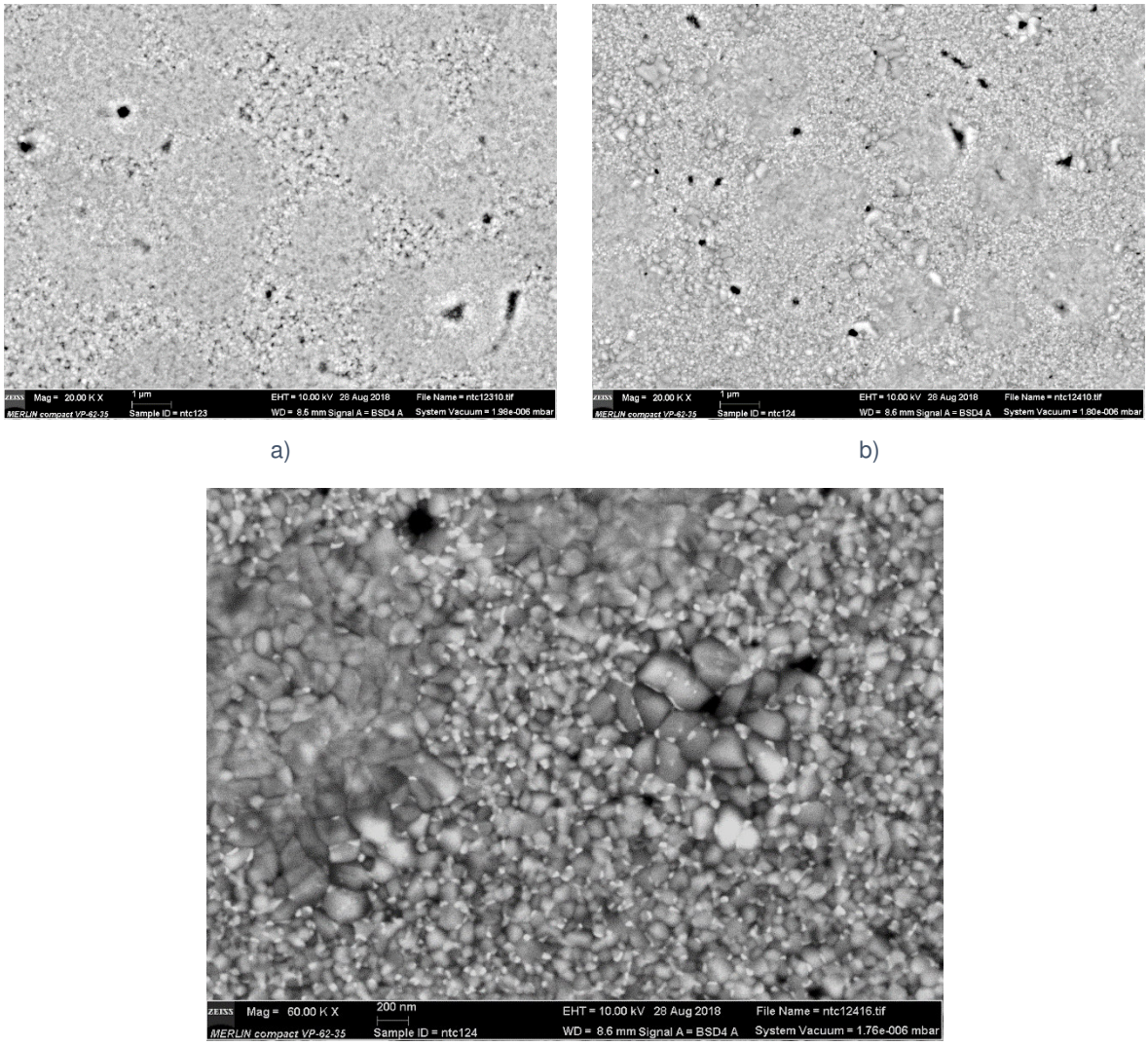

a) b)

c)

Figure 24: BSE images of a 10-air (a) and a 5air+5N2 (b) processed sample. c) BSE image of a section of b) at three times higher magnification. The small bright spots correspond to Ni rich precipitates as already observed for the 5air+5N2 process at 900 °C.

4.2.3 XRD

XRD spectra of one sample from each process run at 750 °C top temperature and a spectrum of a bare Al_2O_3 substrate are displayed in Figure 25. The spectra are labelled and arranged as described in section 4.1.3. 'S' denotes reflections assigned to the spinel phase, 'M' reflections of Mn_2O_3 and '*' is used to label peaks corresponding to the Al_2O_3 substrate.

As proposed by the phase diagram the spectra of the samples processed in air show reflection of the nickel manganite spinel phase and of Mn_2O_3. This is also in agreement with the results found by SEM. That there is no difference between the spectra of the samples processed in air and the spectrum from the 5-N2-c processed sample might be explained,

like for the 900 °C processes, by the short time that the sample is exposed to reducing atmosphere.

The most remarkable features are again found in the spectrum of the 5air+5N2 process. Apparently, the Mn_2O_3 reflections present in all other spectra are missing in the spectrum of the 5air+5N2 processed sample. It is assumed that Mn_2O_3 is formed during the ramp-up and the first half of the hold time which are carried out in air and then reduced to a Mn rich spinel phase during the second half of the hold time and the cooling in nitrogen. As found for this process at 900 °C the spinel peaks are slightly shifted to lower angles which indicates the presence of a Mn rich, tetragonally distorted spinel. This supports the idea of Mn_2O_3 being converted to spinel and also that the Ni rich precipitates found by SEM correspond to NiO which, within the limits of this work, cannot be detected by XRD.

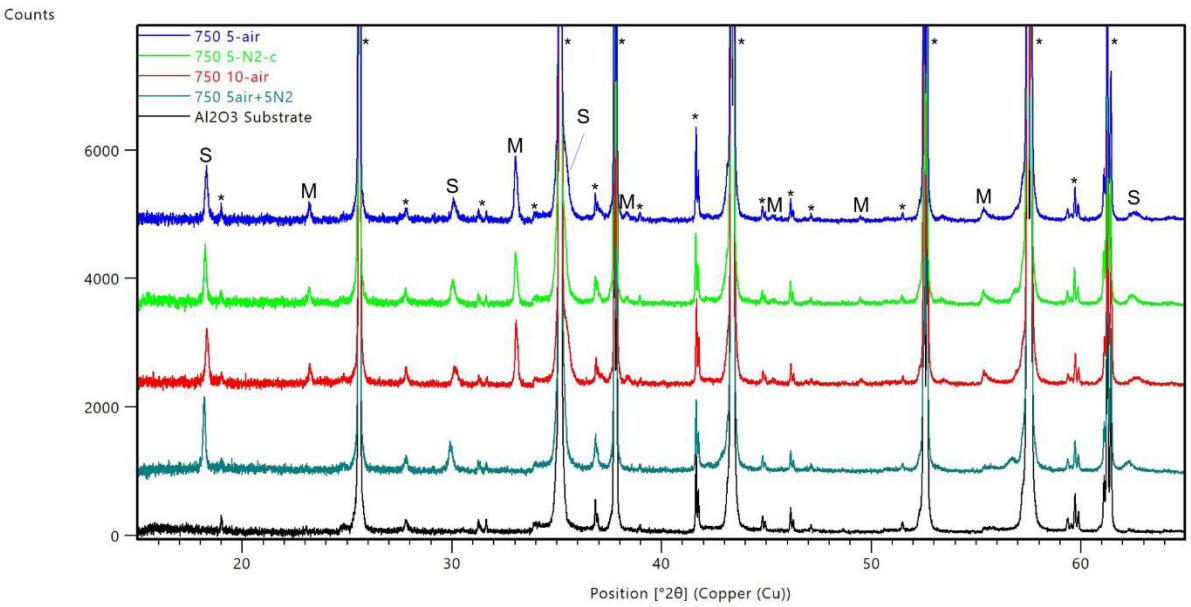

Figure 25: XRD spectra of one sample from each of the four processes run at 750 °C and a spectrum of a bare Al_2O_3 substrate (black spectrum at the bottom). The labelling of the peaks in the topmost spectrum is valid for the spectra shown below as well, of course provided that the peak is present. '*'denotes reflections assigned to Al_2O_3, reflections assigned to nickel manganite spinel are labelled 'S' and reflections of Mn_2O_3 'M'. To enable better comparison counts were manually added to the spectra, thus the scale on the y-axis does not give absolute measured intensity of the reflection but can only be used to compare the relative height of peaks

4.2.4 Electrical Properties and Aging

4.2.4.1 R(T) Measurements

Figure 26 shows the measured resistance (a) and the calculated B values (b) of the samples processed at 750 °C. The data is arranged and presented as described in section 4.1.4.1 on the 900 °C crystallized samples.

The samples processed with the 5-air, 5-N2-c and the 10-air process display very similar resistance and B values. This is in accordance with the findings of the structural characterization which did not yield significant differences between those three processes. The higher resistance of the 5air+5N2 processed samples can be explained by the presence of the Ni rich precipitates. The precipitation of the Ni rich second phase leads to a lower amount of Ni^{2+} in the spinel phase which again leads to a lower number of Mn^{4+} ions on the octahedral positions. Thus, the Mn^{3+}/Mn^{4+} ratio, and hence also the conductivity, decreases.

The fact that the resistance of the samples crystallized at 750 °C is nearly one order of magnitude lower than that of the 900 °C processed samples cannot be explained easily. If the degree of inversion, and the fact that not necessarily all Mn^{3+}/Mn^{4+} ions take part in the charge transfer process are neglected and assumed that all Ni^{2+} ions are located on octahedral sites, the maximum conductivity would be achieved with a Ni content of x = 0.66 which corresponds to a Ni/Mn ratio of 22/78 since then an equal amount of Mn^{3+} and Mn^{4+} would be present on octahedral positions which according to equation (3) leads to the highest conductivity. The composition of the spinel phase in the 900 °C crystallized samples is closer to this ideal value than that of the spinel phase in the 750 °C crystallized samples, thus the 900 °C crystallized samples should display a lower resistance. The fact that a completely different behavior is observed suggests that the spinel phase in the thin films is extensively disordered and that the degree of inversion has a major influence on the resistivity of the NTC thin films.

Another remarkable fact is that the 5-air and the 5-N2-c processed samples show similar resistance values, although there is a significant difference in the obtained film thickness between the two processes (s. section 4.2.2.1). This implies that either the resistivity of the differently processed films differs such that the difference in thickness is compensated or that small deviations in the film thickness do not greatly influence the resistance of the devices. A valid proposition cannot be made at this point and further research is necessary to investigate the relation between the film thickness and the resistance for the given material system and processing route.

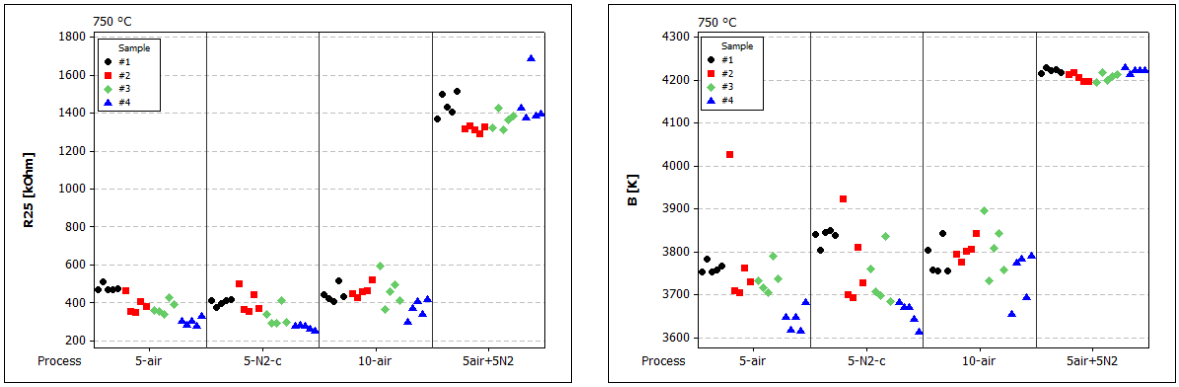

a) b)

Figure 26: a) Resistance of the samples processed at 750 °C measured at 25 °C. Each vertical section of the diagram corresponds to one process. The individual samples of one process can be distinguished by the color and shape of the data points. The devices belonging to one sample are arranged from left to right: device 12, 21, 22, 23, 32. b) Shows the corresponding B values calculated from the resistance at 25 °C and 100 °C

4.2.4.2 Aging

The results of the aging test of the devices fabricated at 750 °C are shown in Figure 27 (ΔR25) and Figure 28 (ΔB).

As found for the samples crystallized at 900 °C the 5-N2-c devices display a slightly lower resistance drift than the 5-air devices but again, due to the spreading this cannot be termed to be significant. The samples of these two processes show a high resistance drift, all devices change their resistance more than 20 %, and no flattening of the aging curves could be observed within 1000 hours.

The devices from the 10-air process show a much better aging behavior. After 500 hours a plateau is reached and almost no further resistance drift is observed between 500 and 1000 hours. It seems that a prolonged hold-time at the top temperature significantly improves the aging stability of the ceramics. In contrast to the 10-air process at 900 °C, the longer hold time did only enhance the aging stability but not influence the initial resistance before aging compared to the 5-air process.

The devices of the 5air+5N2 process at 750 °C show the lowest resistance drift of all processes investigated within this thesis after 1000 hours of aging. All devices of this process show a resistance drift well below 10 % after 1000 hours. The aging curves already flatten after 250 h. Some of the devices even show a resistance decrease after 250 h. However, again the question arises whether this slight resistance decrease is not rather related to uncertainties of the measurement than to the actual development of the ceramics resistivity.

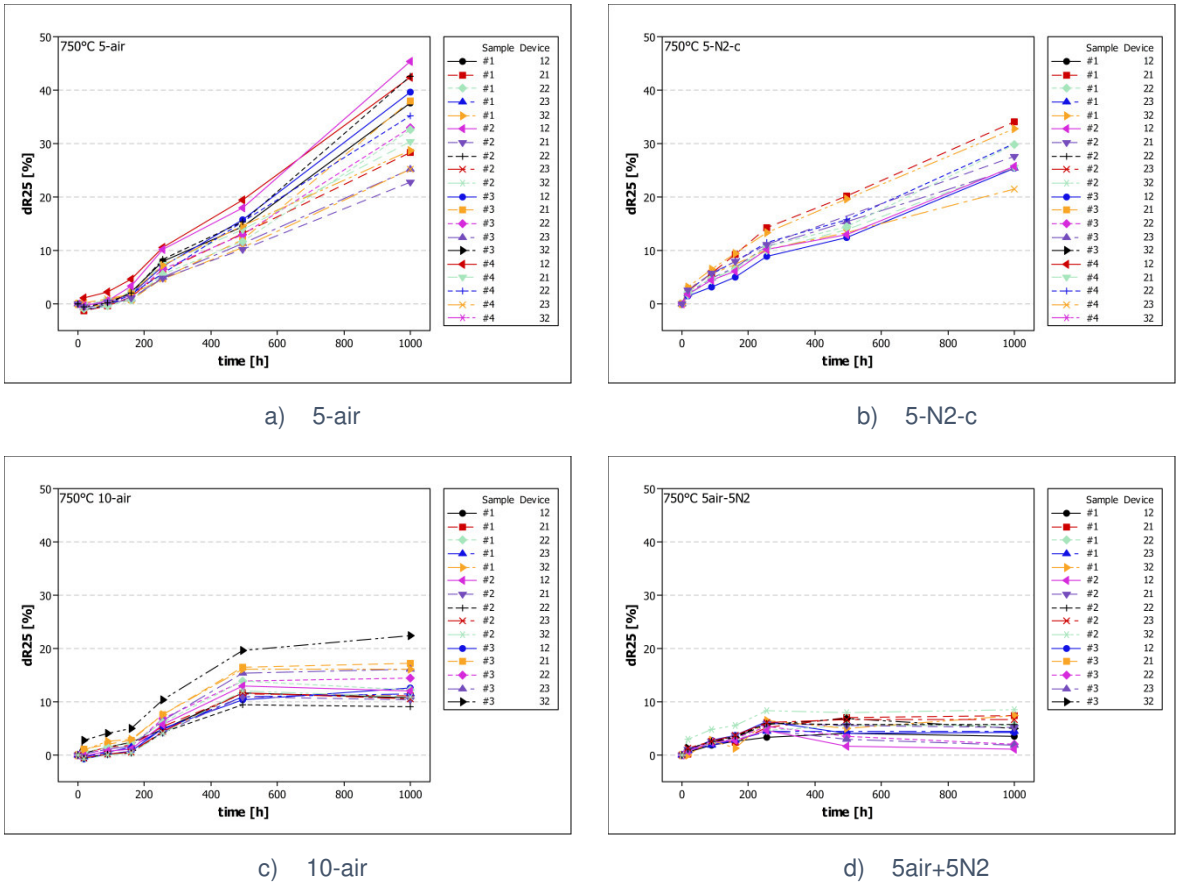

a) 5-air b) 5-N2-c

c) 10-air d) 5air+5N2

Figure 27: Resistance drift of the samples fabricated by the different processes at 750 °C as a function of aging time.

The gradual increase of the B value of the 5-air and 5-N2-c devices over the period of the aging test implies that a gradual change in the thin film material takes place during the storage at elevated temperature. This can be stated since the B value mainly depends on the material itself and is, in contrast to the resistance, independent of geometrical parameters. The devices from the 10-air and the 5air+5N2 process do not display this gradual increase which confirms the higher stability of the thus processed thin films. However, the obtained data does not allow speaking in favor or against one of the aging mechanism introduced in chapter 2.4.

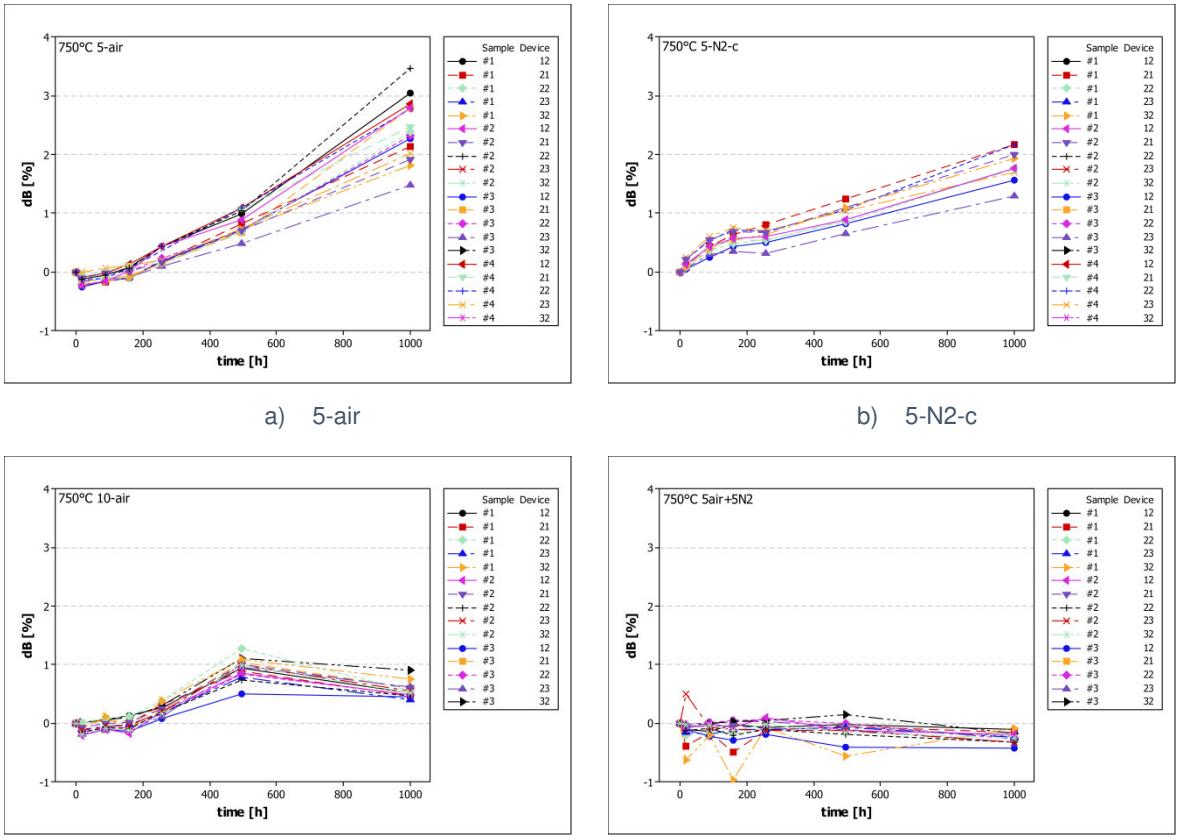

a) 5-air

b) 5-N2-c

c) 10-air

d) 5air+5N2

Figure 28: Drift of the B-value ΔB of the samples fabricated at 750 °C as a function of aging time.

4.3 650 °C Crystallization Temperature

4.3.1 Optical Microscopy

Optical microscopy yielded quite similar results for all processes run at 650 °C crystallization temperature. The films fabricated with the ten-minute hold-time processes partly showed the white spots which are already known from the 5-air process at 750 °C. No white spots were found on the samples fabricated with the five-minute hold time processes. This suggests that the appearance of the white spots, which were identified as circular shapes in SEM, does not depend on the atmosphere and the hold time during crystallization. It might be dependent on the crystallization temperature since the white spots were never encountered on 900 °C crystallized samples. It seems likely that the formation of these defects is related to the CSD process and might be connected to the wetting properties of the precursor and the substrate.

Nearly all thin films crystallized at 650 °C, independent of the process used, showed darker and brighter areas which are visible in optical microscopy as well as with the unaided eye when the sample is viewed against a light source. An example is given in Figure 29 where images recorded in different areas of one single 5air+5N2 processed sample are shown. As can be seen there is not much difference between the bright and the dark area, except for the color. Generally, the optical microscopy images of samples processed at 650 °C showed more variations between each other than the images of samples fabricated at higher temperature. In addition, the observed differences could not be related to the process used but rather appeared between the individual samples without any particular correlation.

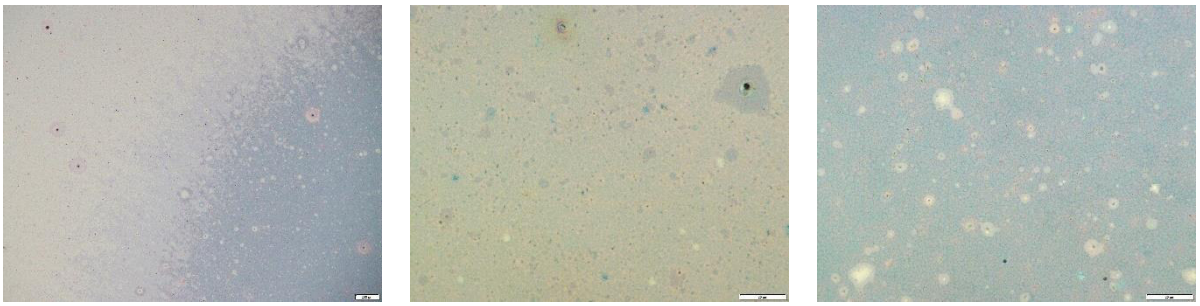

a) b) c)

Figure 29: Optical microscopy images of a 5air+5N2 crystallized sample. a) Transition zone between the bright (left) and the dark (right) area at 50x magnification. b) Detail of the bright area at 1000x magnification. c) Detail of the dark area at 1000x magnification.

4.3.2 SEM

Due to the inhomogeneity of the samples crystallized at 650 °C the following section is structured a little different than the chapters on the 900 °C and 750 °C processes. It was found that it is not possible to relate a certain appearance of the microstructure to a certain

fabrication process, thus ordering according to the process does not make sense. First, as usual, cross section images and film thickness measurements are given. Then a series of SEM and optical microscopy images recorded on different areas of one single sample are shown. At the end the results for the 5air+5N2 process are given.

4.3.2.1 Cross Sections

SEM images of the cross section of a 5-air and a 5-N2-c processed sample were recorded. One representative image of each process is shown Figure 30. The films are not completely dense and pores are visible within the films. In comparison to the samples fabricated at 750 °C the pores are now not only located in the center of the cross sections but at various positions along the thickness of the films. The surface of the films appears to be less smooth and more porous than that of the films crystallized at higher temperature.

The thickness was measured as described in 4.1.2.1 and the following values were obtained:

$t_{650\text{-}5\text{-}air} = (258 \pm 9)\ nm$ and $t_{650\text{-}5\text{-}N2\text{-}c} = (186 \pm 9)\ nm$.

As already observed on the 750 °C treated samples the thin film cooled in nitrogen is significantly thinner than the film processed completely in air. Again no definite explanation for the reason of the thickness differences can be given.

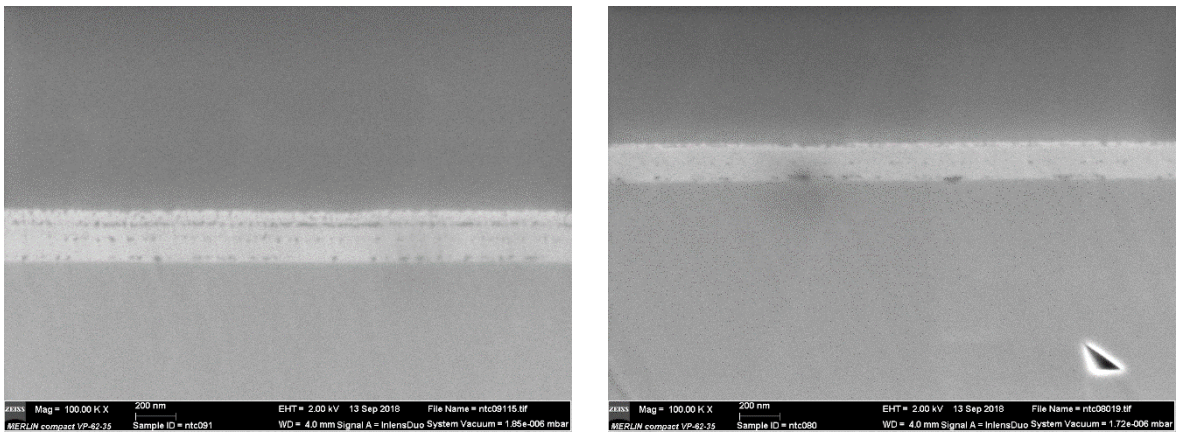

a) b)

Figure 30: a) Cross section of a 5-air processed sample. b) Cross section of a 5-N2-c processed sample.

4.3.2.2 SEM Images and EDS

For a better understanding of the following SEM images and EDS quantification results the results of the XRD measurements which are displayed and explained in section 4.3.2.3 are anticipated here. The films fabricated by the 5-air, 5-N2-c and 10-air processes show strong reflections for Mn_2O_3 and weak for spinel. The films fabricated by the 5air+5N2 process display relatively strong spinel peaks and only very weak peaks for Mn_2O_3.

On a sample of the 5-N2-c process the boundaries of the bright and dark areas were marked with a pen in order to be able to differentiate between the areas in SEM. The sample including the drawn boundary lines is shown in Figure 31. BSE and optical microscopy images of each area are given in Figure 32. In each BSE image the zones where the highest and the lowest concentration of Ni were found by EDS are indicated by the numbered rectangles. The results of the EDS quantification of the zones are given in Table 9.

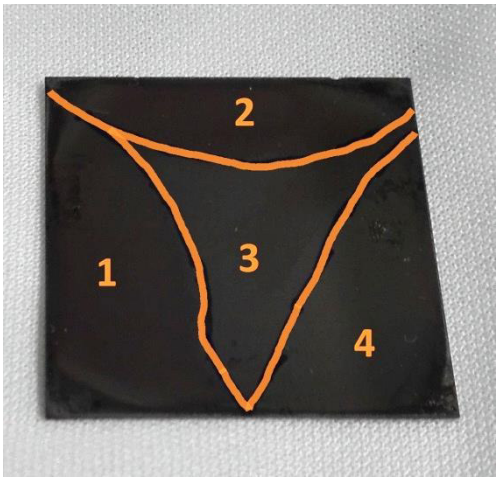

Figure 31: 5-N2-c processed sample with differently bright and dark areas. The boundaries of the areas were marked with a pen to be able to distinguish between them in SEM. Optical microscopy and SEM images of the individual areas are shown in Figure 32. For this image the lines were redrawn on the computer to enable better visibility.

Figure 32 shows that optical microscopy can be misleading when applied for the characterization of the microstructure of the thin films. Area 2 and 3 which look quite different in optical microscopy show nearly the same microstructure in SEM. The only difference between the two areas and area 1 is that in area one the bright, Ni rich regions are a bit larger and more distinct. The only area that shows a significantly different microstructure in SEM is area 4 in which no separated Ni rich and Ni poor areas were found.

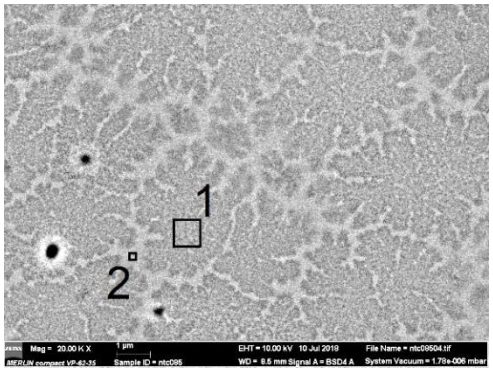

a) Area 1

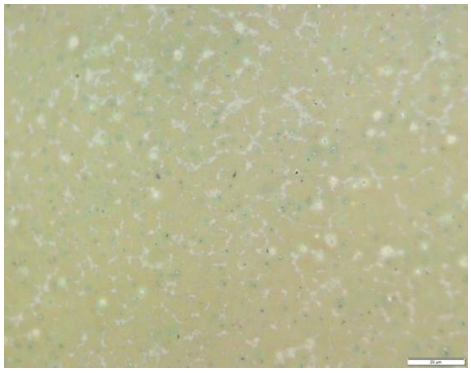

b) Area 1

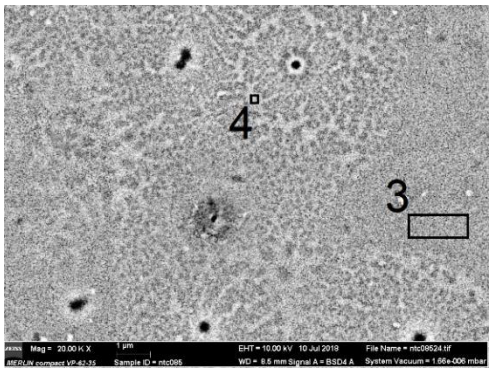

c) Area 2

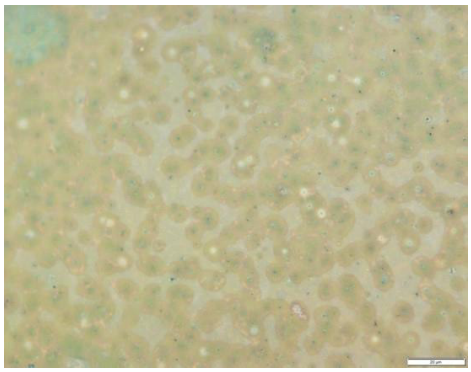

d) Area 2

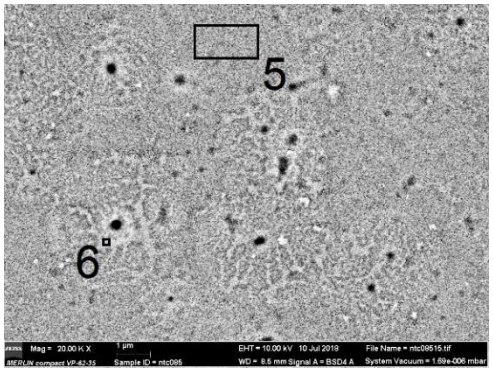

e) Area 3

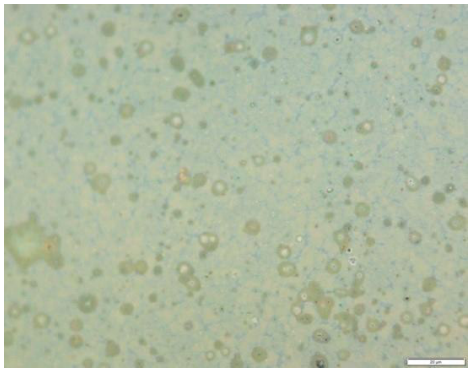

f) Area 3

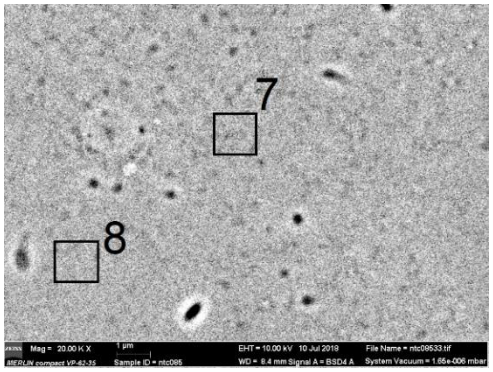

g) Area 4

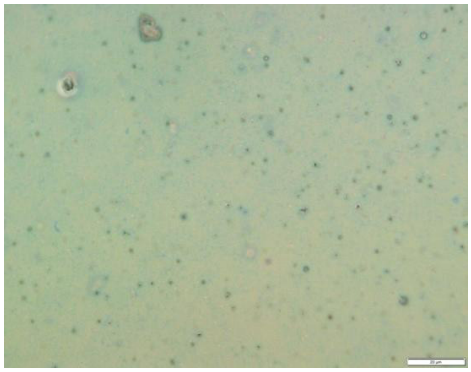

h) Area 4

Figure 32: SEM BSE images (left column) and optical microscopy images (right column) of the differently appearing areas on the 5-N2-c processed sample shown in Figure 31. The numbered rectangles in the BSE images indicate the zones where the highest and lowest concentration of Ni was found by EDS. The results of the quantification are shown in Table 9.

Table 9: EDS quantification results for the numbered zones indicated in the subfigures of Figure 32. Only the elements Mn and Ni were considered for the quantification. A measurement and quantification error of ± 2 at% is assumed.

Subfigure	Zone	Mn [at%]	Ni [at%]
a	1	79	21
a	2	58	42
c	3	75	25
c	4	59	41
e	5	76	24
e	6	58	42
g	7	73	27
g	8	76	24

It is believed that the Ni rich regions correspond to the spinel phase, the Ni poor to Mn_2O_3.The relatively high concentration of Ni in the Mn_2O_3 region, which should not contain Ni at all can be explained with the help of the BSE image of a 10-air sample displayed in Figure 33a. The sample shows a similar microstructure than found in Figure 32a. The image was recorded at twice as high magnification than the BSE images given in Figure 32. As can be seen the darker region consists of very small, fine dispersed bright and dark grains. The Ni rich bright grains are as bright as the big ones which indicates that the composition is about the same. Thus, it can be concluded that the darker regions (zone 1) of Figure 32a consist of a mixture of small spinel grains which have about the same composition as the large spinel areas (zone 2) and small grains of Mn_2O_3. The EDS spectrum and quantification of zone 1 can then be seen as the sum of the signals from a spinel phase with a Ni to Mn ratio of about 40 to 60 and a Mn_2O_3 phase.

Figure 33b shows a SE image of a 10-air processed sample recorded with low acceleration voltage to enhance surface sensitivity. In comparison to the samples fabricated at a higher crystallization temperature the grains are extremely small and it was not possible to resolve them individually in SEM. The samples fabricated by the other processes at 650 °C display a similar surface morphology.

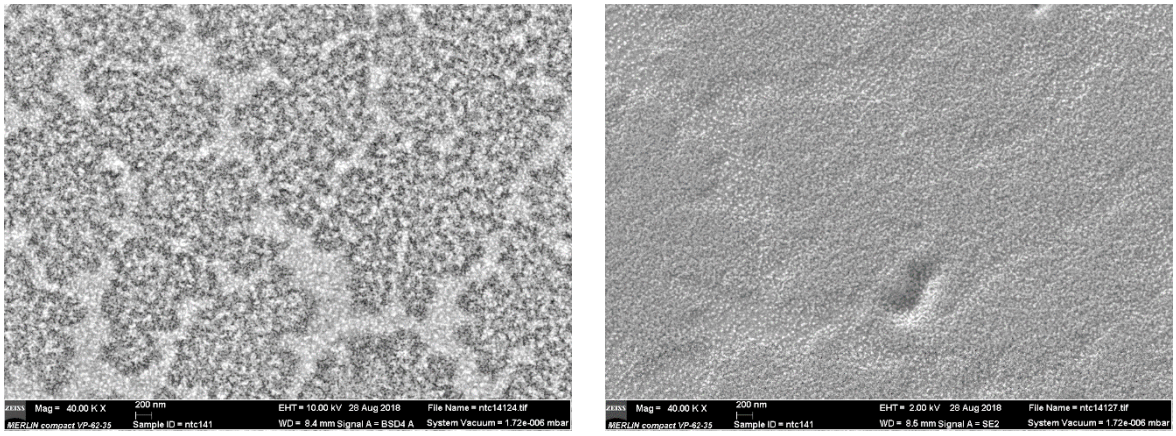

a) b)

Figure 33: a) BSE image of a 10-air processed sample which shows a similar microstructure than found in area 1 of the 5-N2-c sample. The magnification is twice as high as in Figure 32a. The areas between the big bright (Ni rich) areas consist of fine dispersed small bright (Ni rich) and dark (Ni poor) areas.
b) Low acceleration voltage SE image of the surface of a 10-air processed sample. The surfaces of the films fabricated with the other processes at 650 °C look similar.

4.3.2.3 SEM and EDS – 5air+5N2 Process

A BSE images and the EDS mapping of the Ni L line of the corresponding area of a 5air+5N2 processed sample are shown in Figure 34. On the first glance the BSE image in which the Ni rich areas usually appear brighter and the EDS mapping seem to contradict each other. The regions which show a higher concentration of Ni in the mapping appear darker in the BSE image. Having a close look on the BSE image recorded at twice as high magnification (Figure 34c) reveals a similar effect as already described in section 4.1.2.4. The area appearing darker in Figure 34a consists of fine dispersed bright spots which most probably are rich in Ni and dark spots which might even correspond to small pores.

As already stated above the XRD analysis (s. section 4.3.2.3 for detailed results) of the 5air+5N2 processed sample yields reflections for the spinel phase and very weak peaks for Mn_2O_3. From the SEM images and the EDS data it hardly possible to deduce which region in the images corresponds to which phase. No distinct signs for NiO precipitates were found either, which of course does not mean that they are not present since they might simply be too small to be resolved by SEM. For this particular process TEM analysis would be necessary to gain more information on the phase distribution.

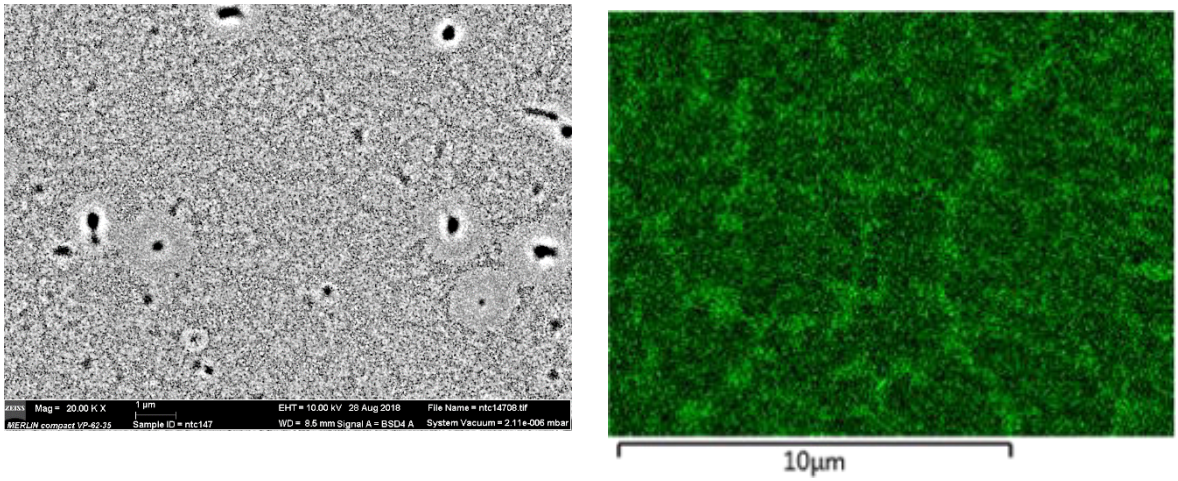

a) b)

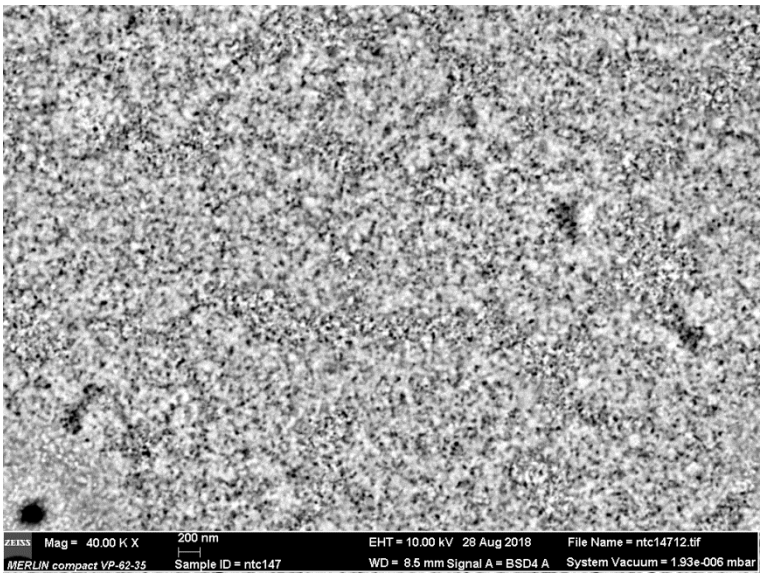

c)

Figure 34 BSE image (a) and EDS mapping of the Ni L line (b) of the same area of a 5air+5N2 processed sample. c) BSE image recorded at twice as high magnification than the image in a. The areas appearing darker in a consist of small bright, presumably Ni rich grains and dark dots which might correspond to pores.

4.3.3 XRD

Figure 35 shows XRD spectra from one sample of each process with 650 °C crystallization temperature and a spectrum of a bare aluminum oxide substrate. The spectra were labelled and arranged as explained in sections 4.1.3 and 4.2.3.

The spectra of the 5-air, 5-N2-c and 10-air process show the same reflections of nickel manganite spinel and Mn_2O_3 as the corresponding samples processed at 750 °C, with the difference that the ratio of the peak heights of the two phases is not the same (s. Figure 25). The reflections corresponding to Mn_2O_3 are relatively strong whereas those of the spinel phase are very weak. It is however remarkable that the spinel phase is observed at all in the

samples crystallized at 650 °C since no spinel phase is predicted by the phase diagram for the given composition and temperature. Schulze et al. [15] who obtained similar results for nickel manganite thin films based on a different precursor system crystallized between 530 °C and 730 °C reasoned that a local change of oxygen partial pressure due to the burn out of residual organics leads to the formation of the spinel phase at such a low temperature. This assumption could neither be proven right nor wrong within the framework of this thesis. However, the results obtained from the 5air+5N2 sample speak in favor of the influence of the atmosphere on the phase composition of the nickel manganite thin film.

The spectrum of the 5air+5N2 processed sample displays similar features as the corresponding sample treated at 750 °C. In contrast to the spectrum of the 750 °C treated sample the peaks of the Mn_2O_3 phase do not disappear completely. The strongest Mn_2O_3 reflection at about 33 2θ angle is, although very weak, still clearly visible in the spectrum of the 5air+5N2 crystallized sample. The same slight peak shift of the spinel reflections, indicating a manganese rich spinel phase, that was already found for the samples of this process crystallized at 900 °C and 750 °C is observable in the spectrum as well.

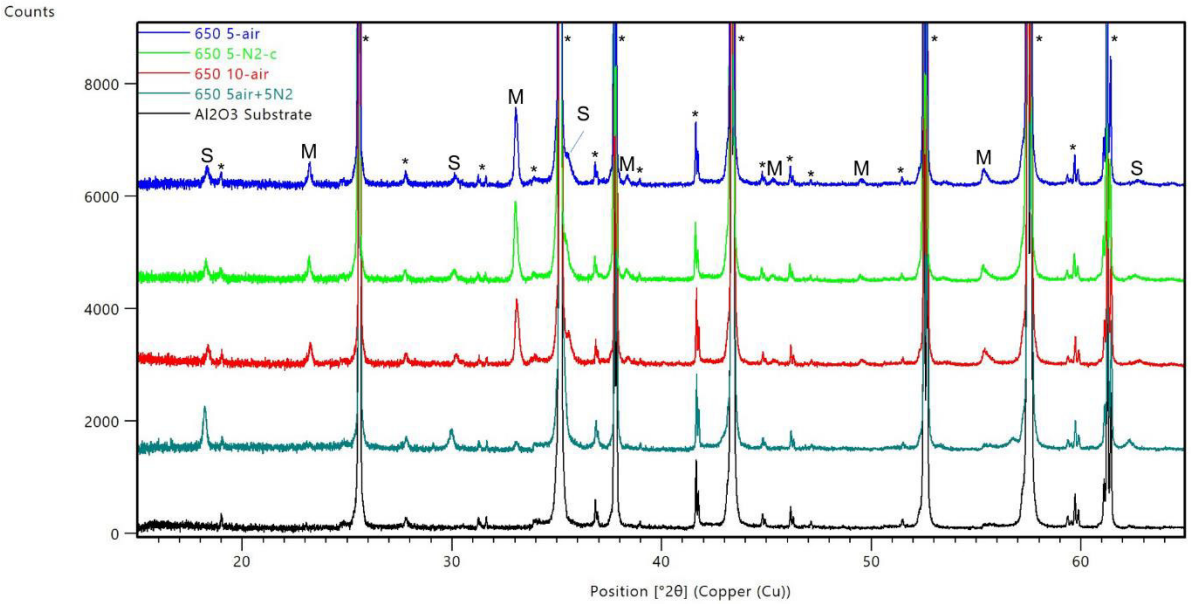

Figure 35: XRD spectra of one sample from each of the four processes run at 650 °C and a spectrum of a bare Al_2O_3 substrate (black spectrum at the bottom). The labelling of the peaks in the topmost spectrum is valid for the spectra shown below as well, provided that the peak is present. '*'denotes reflections assigned to Al_2O_3, reflections assigned to nickel manganite spinel are labelled 'S' and reflections of Mn_2O_3 'M'. To enable better comparison counts were manually added to the spectra, thus the scale on the y-axis does not give absolute measured intensity of the reflection but can only be used to compare the relative height of peaks.

4.3.4 Electrical Properties and Aging

4.3.4.1 R(T) Measurements

The results of the R(T) measurement of the 650 °C crystallized samples are shown in Figure 36. The data is presented and arranged as in the previous two chapters on electrical properties (s. sections 4.1.4.1 and 4.2.4.1).

The electrical behavior of the 650 °C crystallized samples is very similar to that of the 750 °C crystallized ones with the difference that the measured resistance values are about half as high and that the B value of the 650 °C samples is lower. There is no significant difference between the 5-air, 5-N2-c and 10-air processed samples and the samples of the 5air+5N2 process show an about three times higher resistance. This agrees with the results of the of the XRD analysis.

The even lower resistance of the 650 °C crystallized samples in comparison to the 750 °C samples is, as already discussed for the difference between the 750 °C and the 900 °C samples in section 4.2.4.1, not easily explainable by means of the Ni/Mn ratio of the spinel phase. Concerning the film thickness difference between the 5-air and the 5-N2-c process and the nonexistent difference between their resistance values the same reasoning as given in section 4.2.4.1 applies.

Another important point which does not really fit to the low resistance value of the 650 °C crystallized samples is the fact that these films already consist of a considerable amount of insulating Mn_2O_3 phase which should actually not contribute to the charge transport and thus increase the resistance.

At this point it is not possible to coherently explain why the thin films crystallized at lower temperatures exhibit a lower resistance but it is certainly related to the actual cation distribution in the spinel phase and the degree of inversion.

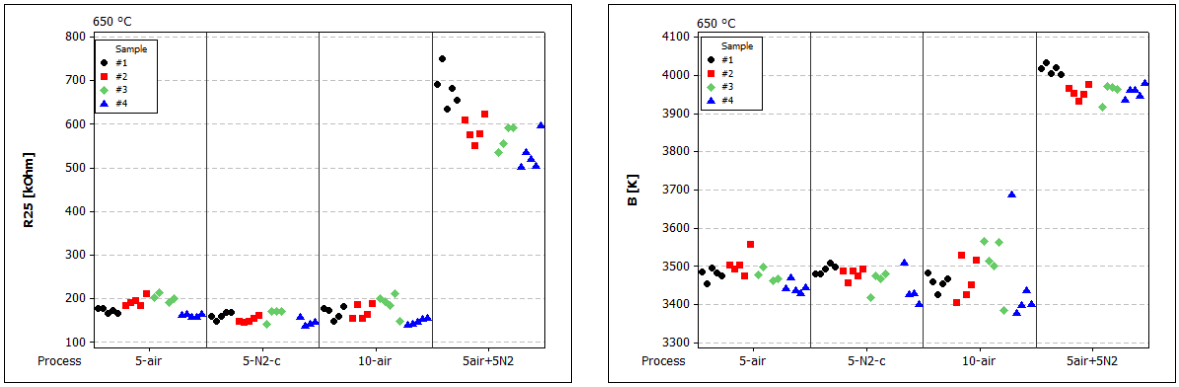

a) b)

Figure 36: a) Resistance of the samples processed at 650 °C measured at 25 °C. Each vertical section of the diagram corresponds to one process. The individual samples of one process can be distinguished by the color and shape of the data points. The devices belonging to one sample are arranged from left to right: device 12, 21, 22, 23, 32. b) Shows the corresponding B values calculated from the resistance at 25 °C and 100 °C

To check whether the dark and bright areas observed on some of the 650 °C crystallized samples affect the resistance, the devices of the 5-N2-c process were analyzed by optical microscopy after sputtering and cutting and it was determined whether a device lies within a dark or a bright region or whether both areas are present on the sample. Since only a small part of the thin film is still visible after sputtering it was only distinguished between brighter and darker regions. No distinction was made between different shades of bright and dark. Figure 37 shows the measured R25 values of the 5-N2-c processed devices. The results are marked according to the appearance of the thin film between the electrodes. As can be seen no correlation between the appearance of the thin film and the measured resistance exists. However, it is believed that this homogeneity issue might become important if the devices are made smaller. This aspect should be taken into account if the geometry of the electrodes is to be downscaled in future research.

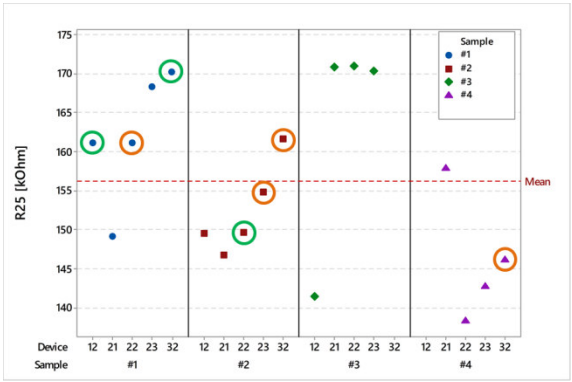

Figure 37: Influence of the dark and bright areas of the 650 °C crystallized samples on the resistance. Devices which lie completely within a dark appearing area are marked by a green, devices which lie within a bright area by an orange circle. Unmarked data points resemble devices on which both colors are present. The horizontal, dashed line denotes the mean R(T) value of all devices.

4.3.4.2 Aging

The drift of the R25 and the B values of the devices fabricated at 650° C during the 1000 h aging test at 150 °C are shown in Figure 38 and Figure 39.

The samples processed at 650 °C show a qualitatively similar aging behavior as the samples fabricated at 750 °C. The devices from the five minute hold-time processes display significantly more severe aging than the devices from the ten-minute hold time processes. No flattening of the aging curves could be observed for the 5-N2-c processed devices. The devices from the 5-air process show a slight flattening of the aging curve between 250 h and 500 h but followed by another steep increase of the resistance drift between 500 h and 1000 h for most of the devices.

In comparison to the devices fabricated at 750 °C no significant difference between the ΔR25 of the 10-air and the 5air+5N2 devices fabricated at 650 °C was found. The majority of the devices from these two processes exhibit a resistance drift between 10 % and 20 % after 1000 h. The aging curves of the 10-air devices are not as steep as those from the five minute hold time processes but no complete flattening was observed over the length of the aging test. The behavior of the 5air+5N2 devices is more difficult to judge since some of the devices still exhibit an increase of the resistance drift, others a decrease and some do not show any change at all between 500 h and 1000 h. Considering the spreading of the individual measurements it might be possible to conclude that, on the whole, no significant further aging occurs for the devices of this process after 500 h at 150 °C.

Concerning the drift of the B value the same considerations as given in section 4.2.4.2 apply.

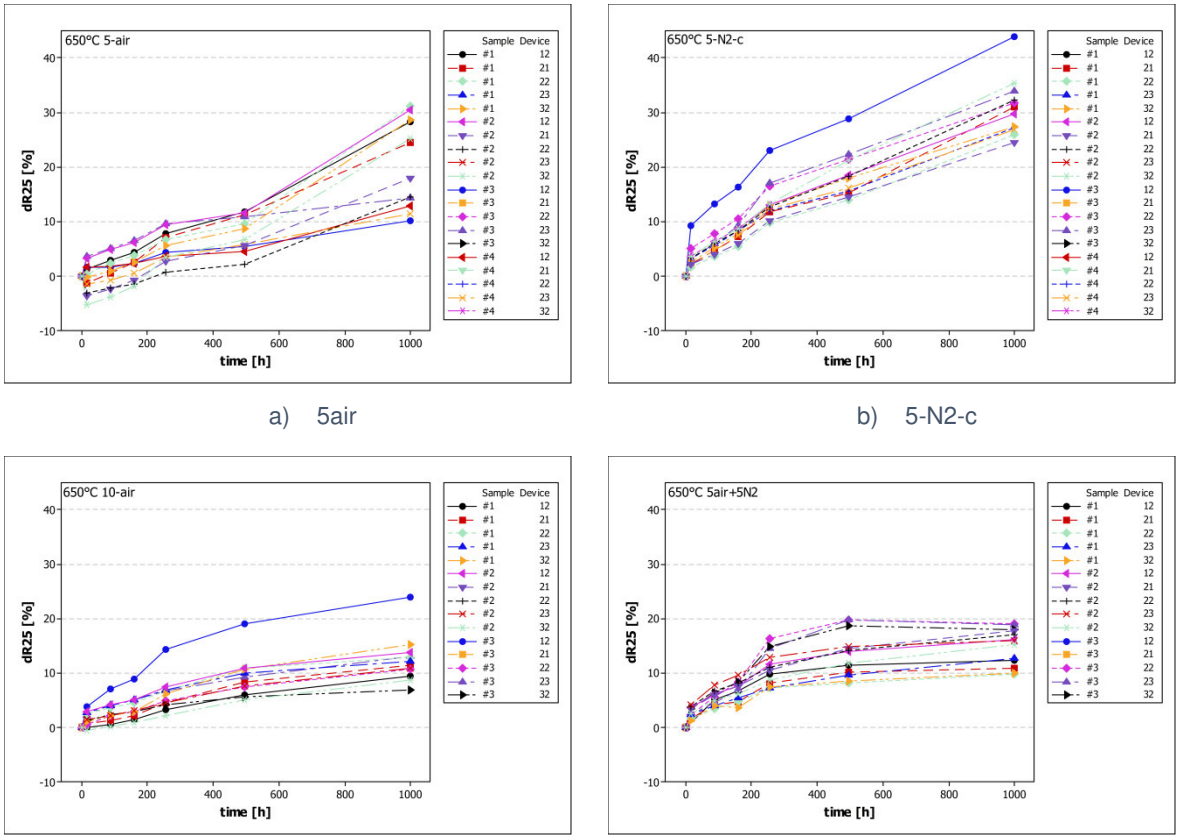

a) 5air

b) 5-N2-c

c) 10-air

d) 5air+5N2

Figure 38: Aging of the samples fabricated by the different processes at 650 °C as a function of aging time.

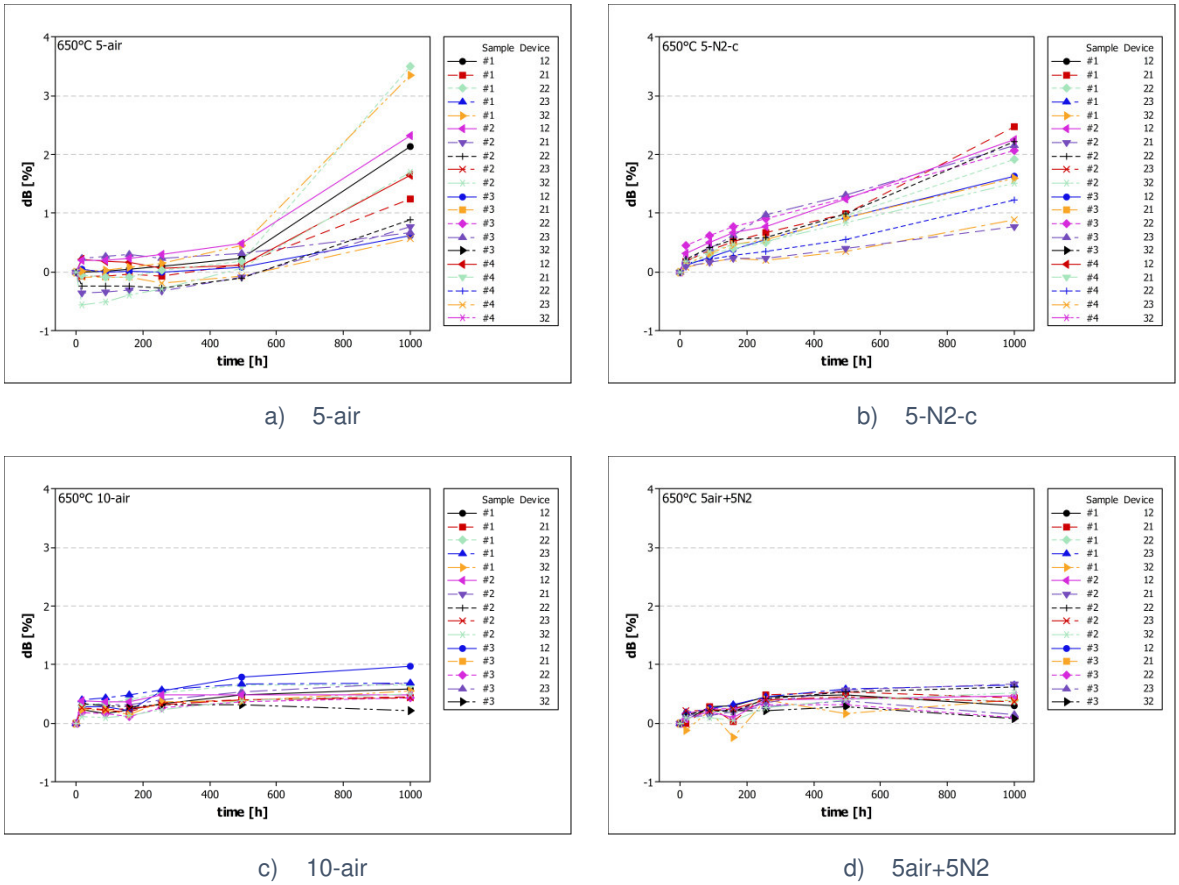

a) 5-air b) 5-N2-c

c) 10-air d) 5air+5N2

Figure 39: Drift of the B-value ΔB of the samples fabricated at 650 °C as function of aging time.

4.4 Summary and Comparison of Electrical Properties

The following graphs give a comparison of the electrical properties of the NTC thin films obtained by the different processes. Figure 40 displays the mean R25 and B values calculated from the data presented in chapters 4.1.4, 4.2.4 and 4.3.4. The error bars indicate the standard deviation of the data. Each subfigure represents one of the processes. As can easily be seen, for each process, the resistance as well as the B value increases with increasing crystallization temperature. It can also be observed that the logarithm of the resistance and the B value are roughly linearly proportional.

Figure 41 presents the mean values of the drift of the R25 after 1000 h aging at 150 °C Again, the error bars correspond to standard deviation of the data. For the samples crystallized at 900 °C and 750 °C the treatment in reducing atmosphere (5air+5N2 process) significantly decreased the resistance drift in comparison to all other processes run at the same temperatures. This effect could, however not be observed with the samples crystallized at 650 °C, where the aging did not significantly differ between the 5air+5N2 and the 10-air process.

Table 10 presents a summary of the mean R25, B and ΔR25 values from all processes.

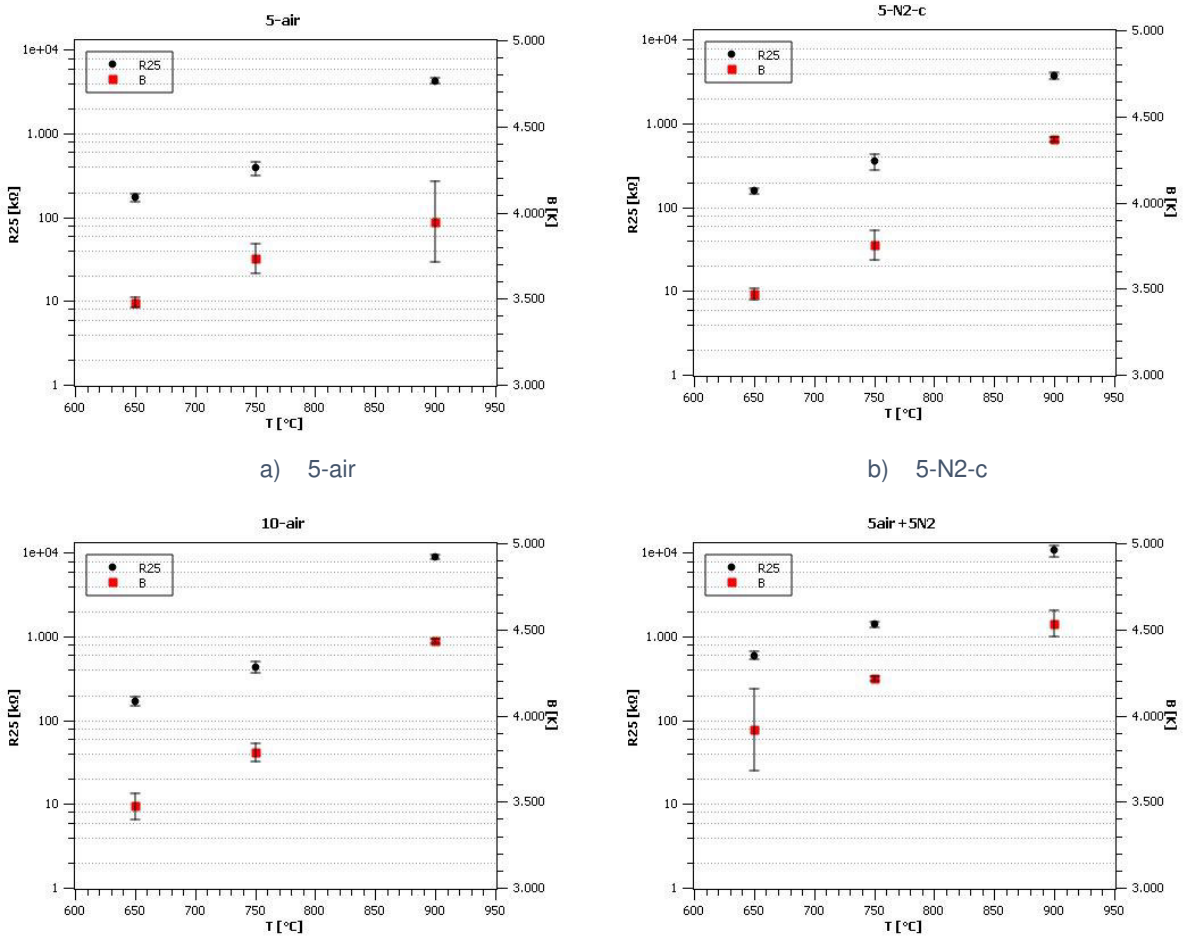

a) 5-air

b) 5-N2-c

c) 10-air

d) 5air+5N2

Figure 40: Mean R25 and B values of the samples fabricated by the different processes at the three different crystallization temperatures. Each quadrant represents one process and shows the obtained electrical properties as a function of crystallization temperature. For better comparability the axis are scaled equally in all four subfigures. The R25 axis (left) is scaled logarithmically, the B axis (right) is linearly scaled. The error bars correspond to the standard deviation of the data.

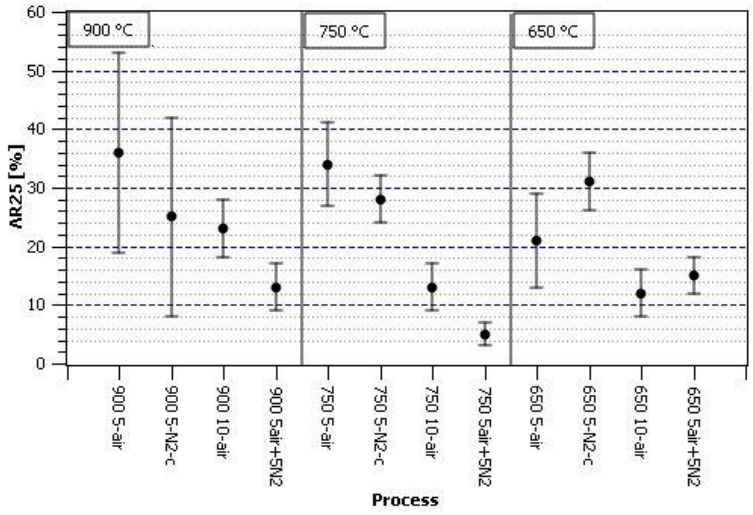

Figure 41 Mean drift of the R25 of the differently processed samples after 1000 h of aging at 150 °C. The error-bars correspond to the standard deviation.

Table 10: Summary of the electrical properties of the NTC thin films.

T	Processing temperature
R25	Mean R25 prior to aging
SD R25	Standard deviation of the R25
B	Mean B value prior to aging
SD B	Standard deviation of B
ΔR25	Mean drift of the R25 after 1000 h of aging at 150 °C
SD ΔR25	Standard deviation of ΔR25 (in percent of ΔR25)

T [°C]	Process	R25 [kΩ]	SD R25 [%]	B [K]	SD B [%]	ΔR25 [%]	SD ΔR25 [%]
900	5-air	4265	8	3947	6.0	36	49
900	5-N2-c	3755	10	4369	0.3	25	66
900	10-air	8838	6	4431	0.3	23	22
900	5air+5N2	10628	15	4533	1.7	13	30
750	5-air	387	19	3732	2.3	34	21
750	5-N2-c	353	20	3750	2.3	28	14
750	10-air	437	15	3784	1.4	13	27
750	5air+5N2	1396	7	4214	0.3	5	45
650	5-air	173	10	3477	0.9	21	38
650	5-N2-c	156	7	3470	0.9	31	17
650	10-air	169	13	3473	2.2	12	34
650	5air+5N2	595	11	3919	6.0	15	22

5 Conclusion

Homogeneous and crack free NTC thin films could be fabricated by CSD on polished aluminum oxide substrates. The pores found by optical microscopy were mainly attributed to pores already existing on the substrates. Inhomogeneities in the optical appearance of the films, mainly encountered on films crystallized at 650 °C, were found to not significantly influence the structural and electrical properties of the thin films.

Depending on the thermal process, NTC thin films with a thickness ranging from 170 nm to 260 nm were fabricated by deposition of six layers and two crystallization steps. SEM images of the cross section revealed that films crystallized at 900 °C were fully dense whereas pores were found within the films crystallized at 750 °C and 650 °C.

For samples processed in air at 750 °C and 900 °C the phase composition of the thin films follows the prediction of Wickham's phase diagram. Single phase nickel manganite spinel films were obtained at 900 °C and mixed phase films consisting of nickel manganite spinel and Mn_2O_3 at 750 °C crystallization temperature. The phase composition of the thin films fabricated at 650 °C in air deviates from the phase diagram. The spinel phase, which is assumed to be responsible for the NTC effect and which, according to the phase diagram, should not exist below 700 °C, was observed. This corresponds to the findings of Schulze et al. [15] who obtained similar results for CSD fabricated NTC thin films based on a different precursor system.

It was found that for each individual process (same hold time and same oxygen partial pressure) the resistance and the B value of the thin films increases with increasing crystallization temperature. A change of the phase composition and/or the degree of inversion in the electrically active spinel phase is considered to be responsible for this effect.

For samples processed completely in air atmosphere at 650 °C and 750 °C doubling of the hold time from five to ten minutes did not significantly change the resistance and the B value of the thin films but did drastically improve the stability of the thin films with regard to aging. For the thin films fabricated at 900 °C in air doubling of the hold time led to an approximately twice as high resistance, an increased B value and only slightly improved the aging behavior. It might be possible that this arises from an interaction of the thin film with the aluminum oxide substrate.

A change from air to nitrogen as processing gas directly at the start of cooling did not significantly change the electrical properties and phase composition of the NTC thin films. Changing the oxygen partial pressure via a change of the processing gas from air to nitrogen after five minutes hold time and keeping the furnace at the top temperature for another five minutes led to an increase of the resistance by approximately a factor of three and an

increased B value compared to the corresponding processes with ten minutes hold time in air. For the samples crystallized at 900 ° the difference between these two processes is smaller since the samples kept for ten minutes in air already exhibited an elevated resistance as mentioned above. For the films crystallized at 750 °C and 900 °C the treatment in reducing atmosphere further improved the aging behavior. However, this trend was not found in the samples crystallized at 650 °C. An exact explanation for this behavior cannot be given at this point. To some extent this observation follows the discussion of Wang et al. [13], who connects oxygen partial pressure during cooling to cation defect concentration, which subsequently triggers changes in the degree of inversion. A closer investigation will be topic of future research.

References

[1] D.G. Wickham, Solid-Phase Equilibria in the System NiO-Mn2O3-O2, J. Inorg. Nucl. Chem. 26 (1964) 1369–1377.

[2] V.F. Balakirev, Y. V. Golikov, Phase equilibrium diagram of the system Ni-Mn-O, J. Phys. Chem. Solids. 49 (1988) 329–332.

[3] G.D.. Csete de Györgyfalva, I.M. Reaney, Decomposition of NiMn2O4 spinel: an NTC thermistor material, Journal of the European Ceramic Society 21 (2001) 2145–2148.

[4] H. Schaumburg, Werkstoffe und Bauelemente der Elektrotechnik, B. G. Teubner, Stuttgard, 1994.

[5] A.J. Moulson, J.M. Herbert, Electroceramics, 2nd edition, Wiley, 2003.

[6] E.G. Larson, R.J. Arnott, D.G. Wickham, Preparation, semiconduction and low-temperature magnetization of the system Ni1-xMn2+xO4, J. Phys. Chem. Solids. 23 (1962) 1771–1781.

[7] S. Fritsch, J. Sarrias, M. Brieu, J.J. Couderc, J.L. Baudour, E. Snoeck, A. Rousset, Correlation between the structure, the microstructure and the electrical properties of nickel manganite negative temperature coefficient (NTC) thermistors, Solid State Ionics. 109 (1998) 229–237.

[8] Yet-Ming Chiang, Dunbar P. Birnie, W. David Kingery, Physical Ceramics: Principles for Ceramic Science and Engineering, Wiley, 1997.

[9] B. Gillot, M. Kharroubi, R. Metz, R. Legros, A. Rousset, Electrical properties and cationic distribution in cubic nickel manganite spinels NixMn3-xO4, 0.57<x<1, Solid State Ionics. 44 (1991) 275–280.

[10] I.G. Austin, N.F. Mott, Polarons in crystalline and non-crystalline materials, Advances in Physics. 18:72 (1969) 41-102.

[11] W.A. Groen, C. Metzmacher, P. Huppertz, S. Schuurman, Aging of NTC Ceramics in the System Mn-Ni-Fe-O, J. Electroceramics. 7 (2001) 77–87.

[12] D.-L. Fang, C.-H. Zheng, C.-S. Chen, A.J.A. Winnubst, Aging of nickel manganite NTC ceramics, J. Electroceramics. 22 (2009) 421–427.

[13] Z. Wang, C. Zhao, P. Yang, L. Winnubst, C. Chen, Effect of annealing in O2 or N2 on the aging of Fe0.5Mn1.84Ni0.66O4 NTC-ceramics, Solid State Ionics. 177 (2006) 2191–2194.

[14] T. Schneller, R. Waser, M. Kosec, D. Payne, Chemical Solution Deposition of Functional Oxide Thin Films, Springer, Vienna, 2013.

[15] H. Schulze, J. Li, E.C. Dickey, S. Trolier-Mckinstry, Synthesis, Phase Characterization, and Properties of Chemical Solution-Deposited Nickel Manganite Thermistor Thin Films, J. Am. Ceram. Soc. 92 (2009) 738–744.